



**fire**  
cci

---


## ESA Climate Change Initiative – Fire\_cci

### D2.2 Algorithm Theoretical Basis Document (ATBD) – SYN

---

<b>Project Name</b>	ECV Fire Disturbance: Fire_cci
<b>Contract N°</b>	4000126706/19/I-NB
<b>Issue Date</b>	19/05/2023
<b>Version</b>	1.1
<b>Author</b>	Amin Khairoun, Joshua Lizundia-Loiola, Emilio Chuvieco, M. Lucrecia Pettinari, Thomas Storm, Martin Boettcher, Grit Kirches
<b>Document Ref.</b>	Fire_cci_D2.2_ATBD-SYN_v1.1
<b>Document type</b>	Public

*To be cited as: Khairoun A., Lizundia-Loiola J., Chuvieco E., Pettinari M.L., Storm T., Boettcher M., Kirches G. (2023) ESA CCI ECV Fire Disturbance: D2.2 Algorithm Theoretical Basis Document-SYN, version 1.1. Available at: <https://climate.esa.int/en/projects/fire/key-documents/>*

	<b>Fire_cci</b> <b>Algorithm Theoretical Basis</b> <b>Document – SYN</b>	Ref.: Fire_cci_D2.2_ATBD-SYN_v1.1	
		Issue 1.1	Date 19/05/2023
		Page 2	

## Project Partners

Prime Contractor/ Scientific Lead & Project Management	UAH – University of Alcalá (Spain)
Earth Observation Team	UAH – University of Alcalá (Spain)
	UPM – Universidad Politécnica de Madrid (Spain)
	CNR-IREA - National Research Council of Italy – Institute for Electromagnetic Sensing of the Environment (Italy)
System Engineering	BC – Brockmann Consult (Germany)
Climate Modelling Group	CNRS - Laboratory for Sciences of Climate and Environment (France)
	VU - Vrije Universiteit Amsterdam (Netherlands)



## Distribution

Affiliation	Name	Address	Copies
ESA	Clément Albergel (ESA)	clement.albergel@esa.int	electronic copy
Project Team	Emilio Chuvieco (UAH)	emilio.chuvieco@uah.es	electronic copy
	M. Lucrecia Pettinari (UAH)	mlucrecia.pettinari@uah.es	
	Amin Khairoun (UAH)	amin.khairoun@uah.es	
	Consuelo Gonzalo (UPM)	consuelo.gonzalo@upm.es	
	Dionisio Rodríguez (UPM)	dionisio.rodriguez@ulpgc.es	
	Ángel García Pedrero (UPM)	angelmario.garcia@upm.es	
	Daniela Stroppiana (CNR)	stroppiana.d@irea.cnr.it	
	Matteo Sali (CNR)	Sali.m@irea.cnr.it	
	Thomas Storm (BC)	thomas.storm@brockmann-consult.de	
	Martin Böttcher (BC)	martin.boettcher@brockmann-consult.de	
	Grit Kirches (BC)	grit.kirches@brockmann-consult.de	
	Florent Mouillot (CNRS)	florent.mouillot@cefe.cnrs.fr	
	Philippe Ciaïis (CNRS)	philippe.ciaïis@lsce.ipsl.fr	
Guido van der Werf (VUA)	g.r.vander.werf@vu.nl		

## Summary

This document presents the technical basis of the algorithms used to generate the Fire\_cci Burned Area derived from Sentinel-3 Synergy data FireCCIS311. The document analyses the input requirements and the process to create the product, including the stages of the processor to get the burned area data and the formatting of the data to obtain the released product.

	<b>Fire_cci</b> <b>Algorithm Theoretical Basis</b> <b>Document – SYN</b>	Ref.:	Fire_cci_D2.2_ATBD-SYN_v1.1		
		Issue	1.1	Date	19/05/2023
				Page	3

	Affiliation/Function	Name	Date
<b>Prepared</b>	UAH	Amin Khairoun Joshua Lizundia Loiola M. Lucrecia Pettinari	19/05/2023
	BC	Emilio Chuvieco Thomas Storm Martin Boettcher Grit Kirches	
<b>Reviewed</b>	UAH – Project Manager	Lucrecia Pettinari	19/05/2023
<b>Authorized</b>	UAH - Science Leader	Emilio Chuvieco	19/05/2023
<b>Accepted</b>	ESA – Technical Officer	Clément Albergel	19/05/2023

This document is not signed. It is provided as an electronic copy.

### **Document Status Sheet**

Issue	Date	Details
<b>1.0</b>	10/03/2023	First issue of the document.
<b>1.1</b>	19/05/2023	Small changes to address review of the Technical Officer

### **Document Change Record**

Issue	Date	Request	Location	Details
1.1	19/05/2023	ESA	Sections 2, 3.1, 3.2, 3.3.1, 3.8.1, 3.11, 3.12, 4	Small changes in the text
			Section 3.11	Prior Section 3.11 (Accuracy assessment) removed.
			Section 5	New reference added.

	<b>Fire_cci</b> <b>Algorithm Theoretical Basis</b> <b>Document – SYN</b>	Ref.:	Fire_cci_D2.2_ATBD-SYN_v1.1		
		Issue	1.1	Date	19/05/2023
				Page	4

## Table of Contents

<b>1. Executive Summary</b> .....	<b>6</b>
<b>2. Introduction</b> .....	<b>6</b>
<b>3. BA Algorithm description</b> .....	<b>7</b>
3.1. General overview of the algorithm .....	7
3.2. Tiling system and calibration sites .....	8
3.3. Algorithm inputs .....	9
3.3.1. Surface Reflectance.....	9
3.3.2. Active fire data .....	10
3.3.3. Land cover.....	10
3.4. Temporal compositing .....	10
3.5. Generation of active fire clusters .....	13
3.6. Selection of potential active fires (PAF) .....	14
3.7. A priori burned patches .....	15
3.8. Establishing cluster-adapted thresholds.....	15
3.8.1. Definition of training samples.....	15
3.8.2. Threshold calculation .....	16
3.9. Estimation of the threshold surface .....	17
3.10. Generation of the final burned area map .....	18
3.11. Uncertainty characterization.....	19
3.12. Date of first detection .....	21
3.13. Current issues and developments of the algorithm.....	22
<b>4. Formatting BA output data to PSD-compliant products</b> .....	<b>22</b>
4.1. Pixel product.....	22
4.1.1. Binning .....	22
4.1.2. The JDAggregator .....	23
4.1.3. Finalisation .....	24
4.2. Grid product.....	25
4.2.1. Sum of burned area .....	25
4.2.2. Ancillary variables .....	26
<b>5. References</b> .....	<b>27</b>
<b>Annex 1: Acronyms and abbreviations</b> .....	<b>31</b>
<b>Annex 2: Sentinel 3 Synergy (S3 SYN) band characteristics</b> .....	<b>33</b>

## List of Figures

Figure 1: Main structure of the FireCCIS311 algorithm. In parenthesis the section where the step was explained. The red dashed box means that those steps were repeated for each active fires spatiotemporal cluster.....	8
Figure 2: Tiling system and calibration areas used to develop the FireCCIS311 algorithm. ....	9

- Figure 3. NBR2 vegetation index and the derived separability  $S$  through different burned pixels distributed along the calibration tiles. In all cases, an active fire was detected in the same location within 0–1 day difference. The locations belong to the following biomes: Mediterranean (1), boreal forest (2, 4), deserts & xeric shrubland (3), and tropical savanna (5, 6, 7). ..... 12
- Figure 4. Monthly variables used by the burned area mapping algorithm: a) active fires spatiotemporal clusters (STC), b) maximum separability ( $S_{max}$ ), c) change in NBR2 of the day with the maximum separability ( $\Delta NBR2_{max}$ ), d) day with the maximum separability ( $t_{max}$ ), e) temporal coherency of the day with the maximum separability ( $\sigma_{t,max}$ ), and f) difference between the day with the maximum separability and the day of detection of the nearest Potential Active Fire ( $\Delta t_{PAF}$ ). The example belongs to September 2019 for an area centred at 18.9° E, 16.7° S in Angola (Africa). ..... 13
- Figure 5. Distribution of the maximum separability ( $S_{max}$ ), maximum separability day vs. active fire day difference ( $\Delta t_f$ ), and texture ( $\sigma_{t,max}$ ) variables derived from 66,186 locations defined by active fires that had an associated burned patch in the reference perimeters. The dashed lines show the global thresholds selected to guide the algorithm. The dark red areas show the regions of the variable where the probability of burn was higher. .... 15
- Figure 6. Definition of the burned (B) and unburned (UB) samples for the active fires cluster (STC) number 27523 located at 18.5°E, 16.5°S (Angola) of September 2019. In c.1 the local zone is defined by a buffer of 10 km around the border of the a priori burned patch intersected by the STC 27523. In c.2, stratum A, B, and C correspond to distances between 10 and 5 km, 5 km and  $R_{AI}$  (i.e., the distance used to create the clusters), and less than  $R_{AI}$ , respectively. Colours in a) just indicate different STC. .... 16
- Figure 7. Threshold surface ( $TH_s$ ) of the  $\Delta NBR2_{max}$  variable generated for the 10° x 10° tile, which encompassed the area between 10°-20° E and 10°-20° S, corresponding to September 2019. .... 18
- Figure 8. Example of predictive variables of uncertainty of FireCCIS310: (a)  $\Delta NBR2_{max}$ ; (b)  $S_{max}$ ; (c)  $\Delta t_{PAF}$ ; (d)  $\sigma_{t,max}$ . .... 20
- Figure 9. Comparison between (a) Reference data and (b) Probability of burn of an area of the tile h19v10 (Angola) for August 2019. .... 21
- Figure 10: (a) Dates of detection of an area of tile h27v02 (Siberia) burned in August. (b) Dates of detection of an area of tile h19v10 (Ghana) burned in December. .... 22
- Figure 11: Calvalus L3 processing ..... 23
- Figure 12: Example of the final layers generated at full pixel resolution for fires occurred in the southern border of Brazil and Bolivia in 2019: (a) Confidence Level (CL) (b) Julian day of detection (JD). (b) Burned Land Cover class (LC). .... 25
- Figure 13. Burned area (km<sup>2</sup>) of the year 2019 detected by the FireCCIS311 product at 0.25° spatial resolution. .... 25

	<b>Fire_cci</b> <b>Algorithm Theoretical Basis</b> <b>Document – SYN</b>	Ref.:	Fire_cci_D2.2_ATBD-SYN_v1.1		
		Issue	1.1	Date	19/05/2023
				Page	6

## 1. Executive Summary

This is the first version of the Algorithm Theoretical Basis Document (ATBD) describing the algorithm used to generate the Fire\_cci global burned area (BA) product derived from Sentinel-3 Synergy. In the previous phase of the contract, a first version of this product for 2019 was released (FireCCIS310). After some minor corrections, the new version 1.1 is produced to extend the time series to the period 2019-2022 (FireCCIS311). This document describes in detail the technical components of the algorithm, the input data used and the released product format.

## 2. Introduction

The ESA Climate Change Initiative (CCI) stresses the importance of providing higher scientific visibility to data acquired by ESA sensors, especially in the context of the Intergovernmental Panel on Climate Change (IPCC) reports. This implies producing consistent time series of accurate Essential Climate Variable (ECV) products, which can be used by the climate, atmospheric and ecosystem scientific community for their modelling efforts. The importance of keeping long-term observations and international links with other agencies currently generating ECV data is also stressed.

Fire Disturbance is one of the ECVs defined by the the Global Climate Observing System (GCOS), mainly due to fire impacts on emissions calculation and carbon budgets. The Fire disturbance ECV identifies BA as the primary fire variable. Accordingly, the Fire\_cci project focuses on developing and validating algorithms to meet the Global Climate Observing System (GCOS) ECV requirements for (consistent, stable, error-characterised) global satellite data products from multi-sensor data archives.

The first algorithm developed within the project used images from the MERIS sensor (Alonso-Canas and Chuvieco 2015). Due to the availability of images from this sensor, the time-series of the MERIS Fire\_cci v4.1 (FireCCI41 to simplify) product only covered the years 2005-2011 (Chuvieco et al. 2016). A new product was released two years later, based on the MODIS sensor (FireCCI50) that extended that time series to the period 2001-2016 (Chuvieco et al. 2018). The algorithm used to obtain this product was developed for the two highest-spatial resolution bands of the MODIS sensor (Red and Near Infrared, NIR) and followed a similar approach to the MERIS hybrid algorithm, as it combined information from hotspots and temporal reflectance changes to detect burned pixels. Differences in the characteristics of both sensors and their derived products (spatial and temporal resolution, view angles, bands characteristics, etc.) and problems found with the FireCCI41 product advised extending the previous developments and introducing some adaptations to the MODIS BA algorithm, which kept improving the thematic and temporal accuracy aspects in the two published versions: FireCCI50 (Chuvieco et al. 2018) and FireCCI51 (Lizundia-Loiola et al. 2020). Nevertheless, the latest algorithm was still showing several limitations. For instance, border effects were still noticeable due to tile-based processing thresholds and the temporal reporting accuracy didn't improve significantly because of the compositing criteria (Liu et al. 2021; Lizundia-Loiola et al. 2021; Lizundia-Loiola et al. 2022). Additionally, cool and small fires observed in sparse vegetation and croplands were highly omitted due to the absence of spectral information in the Short Wave InfraRed (SWIR) region of the spectrum and the use of MODIS 1-km resolution active fires data (Lizundia-Loiola et al. 2022).

	<b>Fire_cci</b>		Ref.: Fire_cci_D2.2_ATBD-SYN_v1.1	
	<b>Algorithm Theoretical Basis</b>		Issue	Date
	<b>Document – SYN</b>		1.1	19/05/2023
			Page	7

The FireCCI51 algorithm is the starting point for the development of the new FireCCIS310 algorithm that initially was going to be applied to the 2017-2019-time series of Sentinel-3 Synergy (SYN) data in Phase 1 of the ESA CCI+ project, following the technical annex submitted to ESA. However, due to the challenges raised in the processing of SYN before 2019, it was decided that the first generation of the FireCCIS310 would be limited to 2019 and then it would be followed by the production of the subsequent years. After the processing of the 2019 dataset, and considering some small issues found in the results (see Subsection 3.13), minor adaptations were introduced to the algorithm, and a new version 1.1 (FireCCIS311) was used to process the 2019-2022 time series.

The objective of this document is to explain the theoretical basis of the algorithm used to generate the new global BA product developed within the frame of the ESA FireCCI project.

### 3. BA Algorithm description

#### 3.1. General overview of the algorithm

The general scheme of the algorithm is summarized in Figure 1 and explained in subsequent sections. The algorithm follows a hybrid approach, which has shown to be one of the most reliable methodologies to detect BA globally (Alonso-Canas and Chuvieco 2015; Campagnolo et al. 2019; Chuvieco et al. 2018; Giglio et al. 2018; Giglio et al. 2009; Lizundia-Loiola et al. 2021; Lizundia-Loiola et al. 2020). Thermal anomalies provide an accurate location and timing of the active fires due to their high thermal contrast with the surrounding areas (Giglio et al. 2016; Schroeder et al. 2014). Conversely, changes in surface reflectance are more persistent both in space and time, providing the chance to detect the entire burned patch. Hybrid algorithms combine the strengths of both thermal anomalies and changes in surface reflectance data to reliably detect BA.

Daily time-series of the vegetation index Normalized Burn Ratio 2 or NBR2 (derived from Trigg and Flasse (2001)) were used to derive a separability index that enhances the burn signal. This separability index was maximised to select within a given month the day with the highest probability of being burned. Based on the selected days, four monthly variables were derived: maximum separability, NBR2 change, texture, and day difference. The texture determined the temporal coherence of adjacent pixels, while the day difference accounted for the consistency between the day of maximum separability and the nearest active fire date. Additionally, active fire clusters were defined considering their spatiotemporal proximity (Lizundia-Loiola et al. 2020). Then, a two-phase methodology (Bastarrika et al. 2011) was applied to detect BA. First, seed pixels were selected based on active fires and cluster-adapted thresholds. This step aimed to reduce commission errors by selecting only those pixels that showed a clear burned signal. In the second step, a contextual growing was applied from the seeds, using the cluster-adapted thresholds to stop it. This last step aimed to reduce omission errors by detecting the entire burned patch. Some of the steps of the algorithm used a global parametrisation to guide the detection process. The definition of those global parameters was based on the reference perimeters that were generated for the calibration areas (Subsection 3.2) and the knowledge coming from other global burned area products.

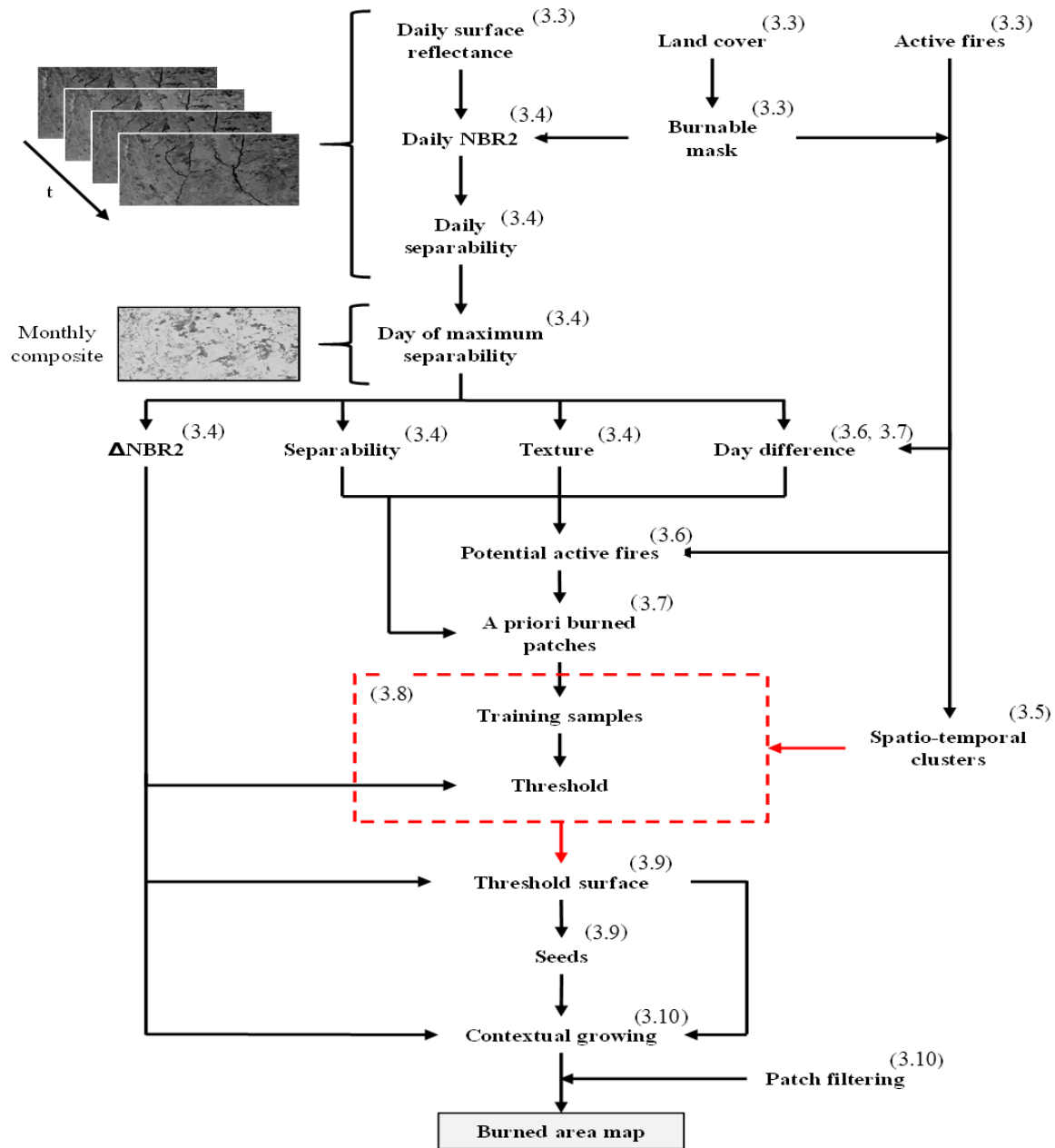


**Figure 1:** Main structure of the FireCCIS311 algorithm. In parenthesis the section where the step was explained. The red dashed box means that those steps were repeated for each active fires spatiotemporal cluster.

### 3.2. Tiling system and calibration sites

The processing units were defined as tiles of  $10^\circ \times 10^\circ$  ( $3600 \times 3600$  pixels) and a total of 273 tiles were processed (Figure 2). The algorithm was initially run for the year 2019 based on SYN images from both Sentinel-3 (S3) A and B. In order to deal with the great diversity of fire regimes found around the world, 13 S3 tiles were selected for algorithm calibration. The selected sites were distributed across the main biomes. Two tiles were located in Canada and included boreal forests. Another two were placed on the western



coast of the United States, in the Mediterranean area of California. Five tiles were located in tropical savannas, the biome with the highest fire activity, but in different continents: one in the Colombian Llanos, two in Africa (one per hemisphere), and two in northern Australia. In Africa another tile was included that encompassed a transition zone between tropical savanna and tropical forest. Additionally, a tile in Kazakhstan was used as representative of deserts and xeric shrublands biome. The last two tiles were placed in Far East Russia and mainly included temperate forests and savannas.

Reference perimeters were generated for 43 Landsat scenes distributed within 12 of the 13 tiles (Figure 2). Landsat 8 images acquired in 2019 were used to extract reference perimeters following the methodology described in Roteta et al. (2021) and Franquesa et al. (2022). Only Landsat pairs where fire activity was observed were interpreted. In the case of the tile located in Colombia, no cloud-free images were available, but it was still used to visually check if any unexpected behaviour arose. For clarification, it should be noted that these reference perimeters were produced ad hoc for the calibration areas and were independent of those used for validation purposes.

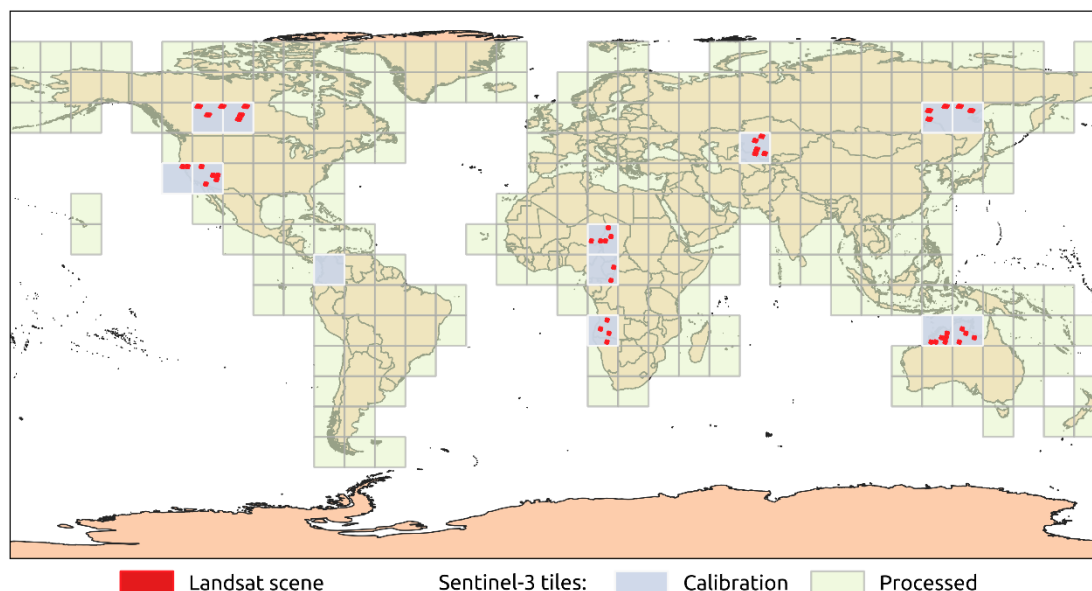



**Figure 2:** Tiling system and calibration areas used to develop the FireCCI51 algorithm.

### 3.3. Algorithm inputs

#### 3.3.1. Surface Reflectance

The main input data sources of the algorithm presented in this document were S3 SYN surface reflectance and Suomi National Polar-orbiting Partnership (S-NPP) Visible Infrared Imaging Radiometer Suite (VIIRS) active fires. Based on the synergistic and co-located measurements of the Ocean and Land Colour Instrument (OLCI) and Sea and Land Surface Temperature Radiometer (SLSTR) optical instruments, the SYN Level 2 product (SY\_2\_SYN) provides surface reflectance and aerosol parameters over land at 300 m for all OLCI and SLSTR bands, excluding OLCI O<sub>2</sub> and Water Vapour absorption bands and SLSTR cloud detection (1374 nm) and thermal bands. This product provides continuity to the surface vegetation products obtained from the VEGETATION instrument aboard the Satellite Pour l'Observation de la Terre (SPOT) and the PROBA-

	<b>Fire_cci</b> <b>Algorithm Theoretical Basis</b> <b>Document – SYN</b>	Ref.:	Fire_cci_D2.2_ATBD-SYN_v1.1		
		Issue	1.1	Date	19/05/2023
				Page	10

V mission. The SYN product is generated for both S3 satellites in operation: S3A (launched in 2016) and B (launched in 2018). These satellites have a near-polar sun-synchronous orbit with an equatorial crossing at 10:00 h (Mean Local Solar Time). The SYN swath is limited to the common area between OLCI and SLSTR swaths (~1270 km), providing a near-daily global coverage from November 2018 onwards. A pre-processing was applied to generate daily composites at 300 m that follow the tiling system shown in Figure 2. When a particular pixel was observed several times during the same day, the most nadiral observation was retained. Among the bands provided by the resulting SYN daily product, two were used to detect burned area: SLSTR band 5 (labelled as SDR\_S5N), which provides information in the short SWIR (SSWIR) centred at 1613.40 nm, and SLSTR band 6 (labelled as SDR\_S6N), which belongs to the long SWIR (LSWIR) centred at 2255.70 nm. A summary of the characteristics of all SYN bands is shown in Annex 2.

### 3.3.2. Active fire data

VIIRS active fires at 375 m resolution were extracted from the VNP14IMGML product (Schroeder and Giglio, 2018), whose time-series begins in January 2012. Compared to the MODIS-based active fire product (MCD14ML Collection 6) that has been used in the existing global BA products (MCD64A1, FireCCI51, C3SBA11), the former product provides enhanced detection of smaller and cooler fires (Oliva and Schroeder 2015; Schroeder et al. 2014).

The VNP14IMGML provides global monthly thermal anomaly location data in ASCII format, along with essential detection information. The files include a layer that specifies the presumed origin of the thermal anomaly: 0 – presumed vegetation fire; 1 – active volcano; 2 – other static land source; 3 – offshore. Of these categories, only the thermal anomalies classified as 0 have been used in the algorithm.

### 3.3.3. Land cover

The only auxiliary data used by the algorithm was the Land Cover (LC) v2.1.1 distributed by the Copernicus Climate Change Service (<https://cds.climate.copernicus.eu/cdsapp#!/dataset/satellite-land-cover?tab=overview>, last accessed January 2023), which is a continuation of the product developed in the Land Cover CCI project (Defourny et al. 2017). This dataset provides global, annual land cover maps since 1992 at 300 m spatial resolution, distinguishing among 22 land cover classes that were defined using the Food and Agriculture Organization’s (FAO) Land Cover Classification System (LCCS). The LC data was used to exclude from further processing the unburnable areas, i.e., regions identified as urban and bare areas, water bodies and permanent snow and ice, and to identify the LC class of the burned pixels in the postprocessing. To represent the situation prior to the fire, the previous year’s land cover map was used.

## 3.4. Temporal compositing

Temporal composites are used in burned area mapping algorithms to overcome problems derived from clouds, angular effects or reception issues found in daily images. These approaches aim to select the best day observation within a certain period, while enhancing the burned signal (Barbosa et al. 1998; Chuvieco et al. 2005; Sousa et al. 2003). They tend to increase the separability between burned and unburned classes to facilitate burned pixel classification (Alonso-Canas and Chuvieco 2015; Giglio et al. 2009). The

	<b>Fire_cci</b> <b>Algorithm Theoretical Basis</b> <b>Document – SYN</b>	Ref.:	Fire_cci_D2.2_ATBD-SYN_v1.1		
		Issue	1.1	Date	19/05/2023
				Page	11

FireCCIS311 algorithm generated monthly composites based on a separability index ( $S$ ) that was derived from a daily time-series of NBR2. The  $S$  index is expressed as:

$$S(t, x, y) = \frac{-\Delta NBR2(t, x, y)}{|\sigma_{pre}(t, x, y) + \sigma_{post}(t, x, y)|/2} \quad (1)$$

$$\Delta NBR2(t, x, y) = NBR2_{post}(t, x, y) - NBR2_{pre}(t, x, y) \quad (2)$$

The NBR2 is a vegetation index, suitable to detect changes from green to scorched or charred vegetation expressed as the normalized ratio between the SSWIR and LSWIR:

$$NBR2 = \frac{\rho_{SSWIR} - \rho_{LSWIR}}{\rho_{SSWIR} + \rho_{LSWIR}} \quad (3)$$

where the corresponding SYN bands used are:  $\rho_{SSWIR} = SDR\_S5N$  (1613.40 nm) and  $\rho_{LSWIR} = SDR\_S6N$  (2255.70 nm).

The separability index  $S$  was first proposed by Giglio et al. (2009) for a vegetation index derived from MODIS NIR-SWIR bands centred at 1240 nm and 2130 nm. In the case of FireCCIS311, this vegetation index is replaced by the NBR2 derived from the SYN SWIR bands. The NBR2 is characterised by a sharp drop after a fire event, leading to low post-fire values (Roteta et al. 2021). It is known for providing high separability between burned and unburned areas, as well as homogeneity within the burned patches, which is an important factor to detect the entire patch (Liu et al. 2021; Roteta et al. 2019).

To obtain the separability for a given day ( $t$ ) and a pixel at location  $(x, y)$ , 16 days with valid observations were needed: eight from the days previous to  $t$  (pre-timeframe) and eight from the days after  $t$  (post-timeframe). In both temporal directions, the selected days have to be the closest in time from  $t$  and, hence, the minimum searching window is of eight days (i.e., from  $t-8$  to  $t-1$  for the pre-timeframe and from  $t$  to  $t+7$  for the post-timeframe). This initial window is progressively extended by  $-1$  in the case of the pre-timeframe and  $+1$  in the case of the post-timeframe until eight days with valid observations are found for each of the timeframes. The maximum searching window is 30 days to ensure that the statistics represented the short-term pre- and post-fire scenarios. If eight valid observations are not found in either of the two timeframes a pixel is labelled as 'non-observed'. This value of eight showed a good balance between a representative estimation of the statistics and the number of non-observed areas (Giglio et al. 2018).

Two summary statistics were computed for the pre- and post-timeframe, using in each case the corresponding eight NBR2 values: the 10% trimmed mean ( $NBR2_{pre}(t, x, y)$  and  $NBR2_{post}(t, x, y)$ ) and trimmed standard deviation ( $\sigma_{pre}(t, x, y)$  and  $\sigma_{post}(t, x, y)$ ). When the number of values is proportional to 10, the 10% trimmed summary statistics exclude the corresponding proportion of the lowest and highest values, e.g., with 10 values the lowest and highest values are excluded leaving eight values to compute the statistic. However, when the number of values is not proportional to 10, weights have to be estimated for each value. In our case, the lowest and highest values are weighted by a factor of 0.2 and the rest by a factor of 1. Finally, the separability for the day  $t$  and pixel  $(x, y)$  is computed as shown in equation (1).

Figure 3 shows the behaviour of both the NBR2 and  $S$  for several burned locations distributed among the calibration areas. A sharp drop in the NBR2, such as those expected to be generated by fires, leads to large positive values of  $S$ . Therefore, monthly composites were generated by maximising  $S$ . To avoid artificial splits of fires that took place at the end or beginning of a month, the monthly composites were generated considering  $S$  values of the last 15 days of the previous month ( $m-1$ ), the days of the month ( $m$ ) being processed, and the first 15 days of the following month ( $m+1$ ). Using these data, the day with the maximum separability was selected for each pixel ( $t_{max}(m,x,y)$ ). The separability ( $S_{max}(m,x,y)$ ) and the change in NBR2 ( $\Delta NBR2_{max}(m,x,y)$ ) of  $t_{max}(m,x,y)$  were stored as well. Figure 4b, c, and d show an example of each of these monthly composites of September 2019 for a region located in Angola.

Since burned patches are expected to have a high temporal coherence in  $t_{max}$  an additional variable, denoted as  $\sigma_{t,max}(m,x,y)$ , is computed (Giglio et al. 2009). This variable is characterised by the standard deviation of  $t_{max}$  within a rook's case window ( $3 \times 3$ ), i.e., pixels at the diagonals are not considered, around each pixel. To avoid the loss of fine (i.e., 1-pixel) sections of burned patches an edge-restoring ranked order filter that selects the 33<sup>rd</sup> percentile within a  $3 \times 3$  window around the pixel is applied (Astola and Kuosmanen 1997) (Figure 4e).

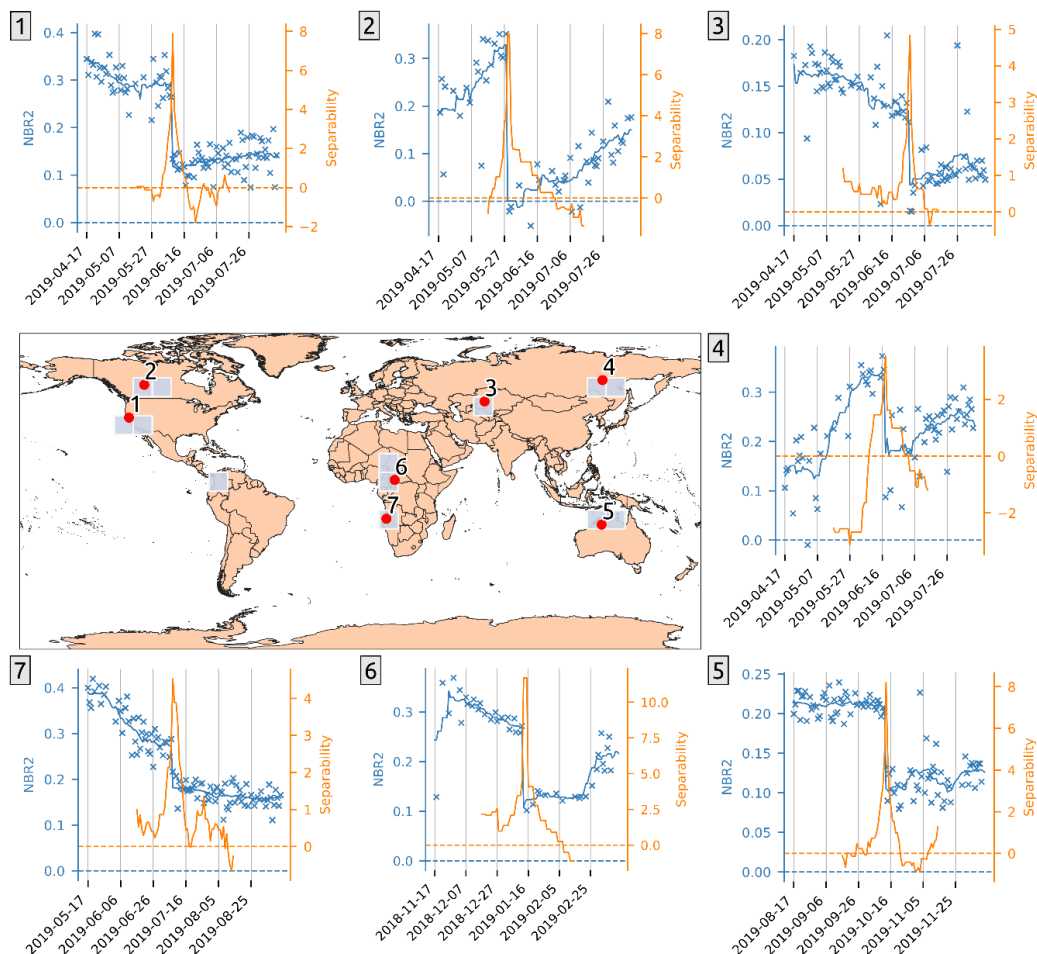


**Figure 3.** NBR2 vegetation index and the derived separability  $S$  through different burned pixels distributed along the calibration tiles. In all cases, an active fire was detected in the same location within 0–1 day difference. The locations belong to the following biomes: Mediterranean (1), boreal forest (2, 4), deserts & xeric shrubland (3), and tropical savanna (5, 6, 7).

### 3.5. Generation of active fire clusters

Following the FireCCI51 algorithm (Lizundia-Loiola et al. 2020), FireCCIS311 uses spatiotemporal active fire clusters (STC) to guide the thresholding process. Each cluster is assumed to represent a fire and, hence, dynamic thresholds for each burned patch are computed by defining cluster-adapted burned and unburned samples (Subsection 3.8). Clusters are created considering the spatial and temporal distribution of the active fires. The spatial distance, also known as the area of influence ( $R_{AI}$ ), proposed by Lizundia-Loiola et al. (2020) to consider two active fires part of the same cluster, is of 1875 m. However, this distance was obtained based on MODIS active fires and was suited for its spatial resolution of 1 km. Therefore, considering the higher spatial resolution of VIIRS active fires used by the new algorithm, the  $R_{AI}$  distance was adapted based on the proportionality of the spatial resolutions of VIIRS and MODIS active fires:  $375 \text{ m} / 1000 \text{ m} * 1875 \text{ m} = 703.125 \text{ m}$ . This adjusted distance was more adequate to address the much higher density of active fires per burned patch that can be found in VIIRS 375 m in comparison to MODIS (Oliva and Schroeder 2015; Schroeder et al. 2014; Waigl et al. 2017). Regarding the temporal difference to consider two active fires part of the same cluster, the original threshold of 4 days proposed by Lizundia-Loiola et al. (2020) is kept since it is related to the characteristics of the fire regimes and not to the sensor's characteristics. Figure 4a shows an example of these STC, where different colours represent different clusters. To increase the overlap between consecutive months, active fires of the last 5 days of the previous month and the first 5 days of the following month were used along with the active fires of the month being processed.

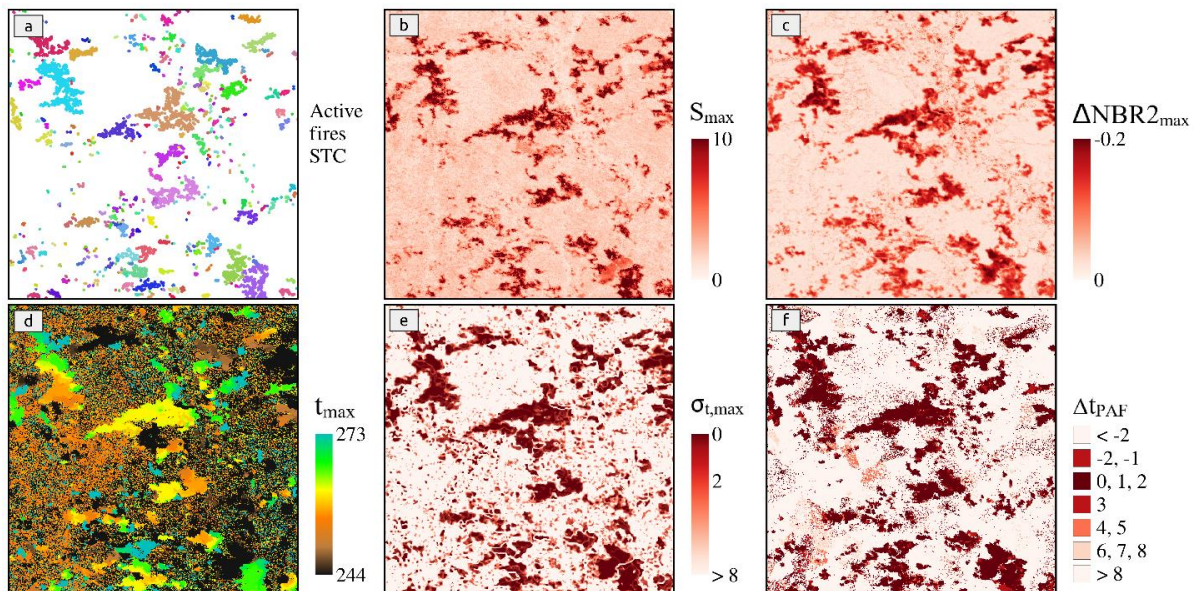


**Figure 4.** Monthly variables used by the burned area mapping algorithm: a) active fires spatiotemporal clusters (STC), b) maximum separability ( $S_{max}$ ), c) change in NBR2 of the day with the maximum separability ( $\Delta NBR2_{max}$ ), d) day with the maximum separability ( $t_{max}$ ), e) temporal coherency of the day with the maximum separability ( $\sigma_{t,max}$ ), and f) difference between the day with the maximum separability and the day of detection of the nearest Potential Active Fire ( $\Delta t_{PAF}$ ). The example belongs to September 2019 for an area centred at  $18.9^\circ \text{ E}$ ,  $16.7^\circ \text{ S}$  in Angola (Africa).

	<b>Fire_cci</b> <b>Algorithm Theoretical Basis</b> <b>Document – SYN</b>	Ref.:	Fire_cci_D2.2_ATBD-SYN_v1.1		
		Issue	1.1	Date	19/05/2023
				Page	14

### 3.6. Selection of potential active fires (PAF)

As explained in the input data section, the VIIRS thermal anomalies product used by the new algorithm provided a “type” field that allows applying an initial filtering of presumed vegetation fires. It might be reasonable to think that due to the low commission rates of active fire products (Schroeder et al. 2014), further filtering was not necessary. However, several key points must be considered when using active fires for burned area mapping. The first and main limitation is set by the spatial resolution of the sensor that is providing the spectral information for burned area detection. In this case, the average SYN pixel is about 300 m, meaning that the smallest burned area that can be detected comprises one that causes a discernible change in spectral reflectance at 300 m resolution, nominally 90,000 m<sup>2</sup>. Conversely, a fire burning at around 650 K with an area of 50 m<sup>2</sup> (night-time case) or 250 m<sup>2</sup> (daytime case) had a 50% probability of being detected by the VIIRS active fire algorithm (see probability curves as a function of fire area and temperature in Schroeder et al. (2014)). This contrast between detection capabilities made it highly probable that fires correctly identified by VIIRS were not able to generate a detectable spectral change in SYN at 300 m resolution. Additionally, it could happen that the “type” field provided by the active fire product is not able to properly classify all thermal sources that are not related to vegetation fires (volcanos, static sources, etc.). Before applying any further filtering process, active fires are relocated in the pixel with the maximum  $S_{max}(m,x,y)$  within a  $3 \times 3$  window around the pixel that fall just below the original location of the active fire. The maximum separability location  $(x',y')$  is assumed to provide a better representation of the actual position of the active fire instead of the original location  $(x,y)$  since the high radiative energy released by the fire might contaminate surrounding pixels. Then, for each relocated active fire, the difference between  $t_{max}(m,x,y)$  and the date of the active fire, defined as  $t_f(m,x',y')$ , is computed ( $\Delta t_f(m,x',y')$ ). The potential active fires (PAF) are selected from the relocated active fires based on the following set of rules:

1.  $S_{max}(m,x',y') \geq 2$
2. Either one of the following conditions was met:
  - a.  $(-2 \leq \Delta t_f(m,x',y') \leq 8)$  AND  $(\sigma_{t,max}(m,x',y') \leq 1)$
  - b.  $(0 \leq \Delta t_f(m,x',y') \leq 2)$  AND  $(\sigma_{t,max}(m,x',y') \leq 8)$

PAF represent not only pixels with a high probability of being burned, but also pixels that are part of burned patches that generate a spectral change at 300 m. The global parameter  $S_{max} \geq 2$  was set based on the distribution derived from 66,186 locations defined by active fires that had an associated burned patch in the reference perimeters. In the cases of texture ( $\sigma_{t,max}$ ) and day difference ( $\Delta t_f$  and  $\Delta t_{PAF}$ ) two ranges were defined based on the same calibration set: a first range of values where the probability of burn was higher (>60% of the active fires fall in this range) ( $\sigma_{t,max} \leq 1$  or  $0 \leq \Delta t_f \leq 2$ ) and a second less restrictive range that was used to confirm the burn ( $\sigma_{t,max} \leq 8$  or  $-2 \leq \Delta t_f \leq 8$ ). Figure 5 shows the distributions and the selected thresholds for each of these variables.

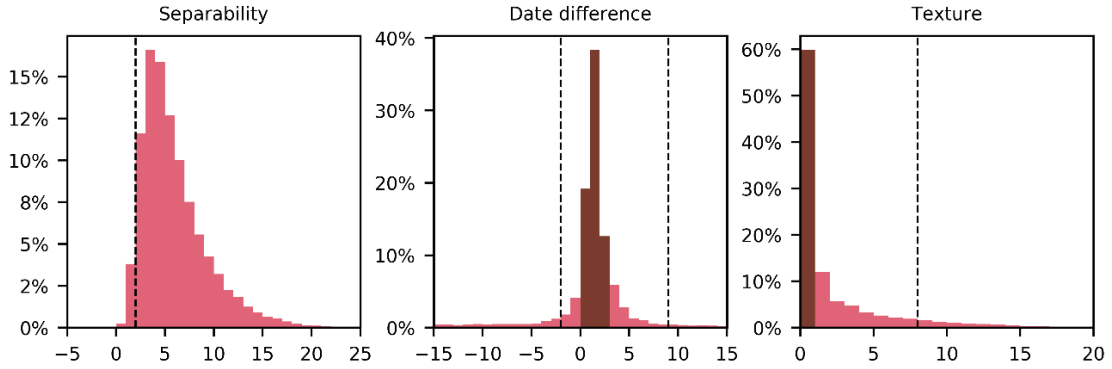


**Figure 5.** Distribution of the maximum separability ( $S_{max}$ ), maximum separability day vs. active fire day difference ( $\Delta t_f$ ), and texture ( $\sigma_{t,max}$ ) variables derived from 66,186 locations defined by active fires that had an associated burned patch in the reference perimeters. The dashed lines show the global thresholds selected to guide the algorithm. The dark red areas show the regions of the variable where the probability of burn was higher.

### 3.7. A priori burned patches

At this point, the  $\Delta t_f(m,x',y')$  variable, which provide valuable information to quantify the temporal uncertainty, is extended to the whole tile. To do that, the  $t_f(m,x',y')$  of the nearest PAF is assigned to each pixel of the image based on Thiessen polygons (Brassel and Reif 1979), obtaining  $t_{PAF}(m,x,y)$ . Then,  $\Delta t_{PAF}(m,x,y)$  is calculated as the difference between  $t_{max}(m,x,y)$  and  $t_{PAF}(m,x,y)$  (Figure 4f). To define a priori burned patches, a contextual growing was applied, iteratively adding pixels that meet the following conditions:

1. An adjacent pixel in a rook's case window ( $3 \times 3$ ) must be a PAF or a pixel previously identified as part of an a priori burned patch
2.  $S_{max}(m,x,y) \geq 2$
3. Either one of the following conditions must be met:
  - a.  $(-2 \leq \Delta t_{PAF}(m,x,y) \leq 8)$  AND  $(\sigma_{t,max}(m,x,y) \leq 1)$
  - b.  $(0 \leq \Delta t_{PAF}(m,x,y) \leq 2)$  AND  $(\sigma_{t,max}(m,x,y) \leq 8)$

These conditions are similar to the ones used to select PAF, but  $\Delta t_f(m,x',y')$  is replaced by  $\Delta t_{PAF}(m,x,y)$ , so they could be extended to the whole tile. At this step, a rook's case window, which did not consider pixels located in the diagonals, was used as it is more restrictive than a queen's case window (i.e., where diagonals are considered).

### 3.8. Establishing cluster-adapted thresholds

#### 3.8.1. Definition of training samples

Due to the availability of high-resolution active fires data from VIIRS, the definition of a suitable burned sample was more feasible than the definition of the unburned sample. As it was already mentioned, active fire products showed low commission errors while providing accurate positioning and timing of the fire events (Boschetti et al. 2010). Therefore, most of the hybrid algorithms used for burned area detection rely on those locations and their surroundings to define the burned samples (Alonso-Canas and Chuvieco 2015; Chuvieco et al. 2018; Giglio et al. 2018; Giglio et al. 2009; Lizundia-Loiola et al. 2020). In the case of the unburned class, however, it is more difficult to define a sample due to its spectral heterogeneity. A common approach is to consider as

unburned those pixels located further away than a given distance from active fires (Alonso-Canas and Chuvieco 2015; Chuvieco et al. 2018; Lizundia-Loiola et al. 2020).

In our case, training samples were defined for each STC (Figure 6a) to estimate cluster-adapted thresholds, properly expressing local conditions. To define what “local” meant, first, the a priori burned patch (Figure 6b) that was intersected by the PAF of a given STC was selected. Then, a buffer of 10 km was defined from the border of the intersected a priori burned patch, defining thus the local zone (Figure 6c.1). The burned sample, labelled as  $B(m,STC)$ , was composed of pixels that fall within that local zone and belong to any a priori burned patch. The remaining pixels represented the unburned class ( $UB(m,STC)$ ). Figure 6 shows an example of the samples that were selected for a fire at 18.5°E, 16.5°S in September 2019, where in Figure 6c.2 red areas represent  $B(m,STC)$  and green tones  $UB(m,STC)$ . This cluster-based sampling methodology allowed representing local conditions and adapting to different fire regimes that might be present throughout the tile without the need for other auxiliary data (e.g., land cover data) (Lizundia-Loiola et al. 2020).

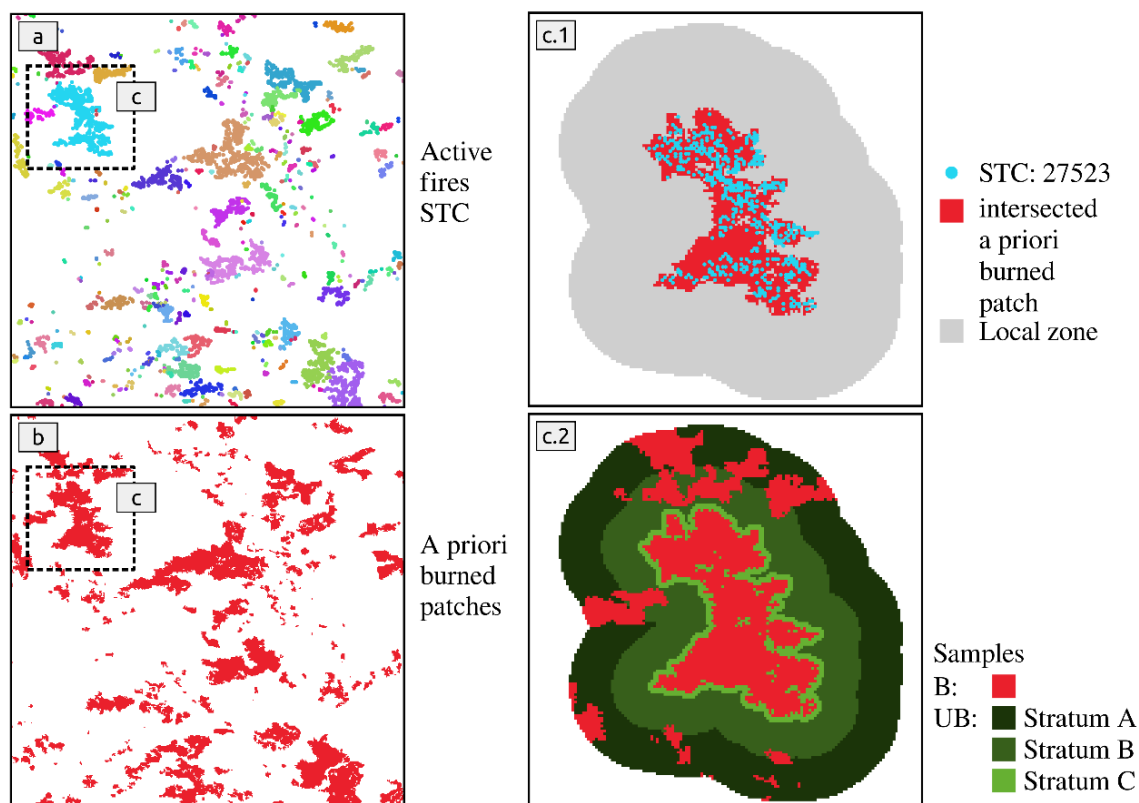


**Figure 6.** Definition of the burned (B) and unburned (UB) samples for the active fires cluster (STC) number 27523 located at 18.5°E, 16.5°S (Angola) of September 2019. In c.1 the local zone is defined by a buffer of 10 km around the border of the a priori burned patch intersected by the STC 27523. In c.2, stratum A, B, and C correspond to distances between 10 and 5 km, 5 km and  $R_{AI}$  (i.e., the distance used to create the clusters), and less than  $R_{AI}$ , respectively. Colours in a) just indicate different STC.

### 3.8.2. Threshold calculation

Obtaining adequate thresholds is crucial for burned area mapping algorithms that rely on contextual growing to detect burned patches. Too restrictive thresholds reduce commission errors, but at the expense of incomplete detections of burned patches. Conversely, too relaxed thresholds may reduce omission errors but at the cost of excessive



	<b>Fire_cci</b> <b>Algorithm Theoretical Basis</b> <b>Document – SYN</b>	Ref.:	Fire_cci_D2.2_ATBD-SYN_v1.1		
		Issue	1.1	Date	19/05/2023
				Page	17

growing and, hence, more commission errors (Alonso-Canas and Chuvieco 2015; Giglio et al. 2009). The FireCCIS311 algorithm used an automatic threshold methodology, called Otsu method (Otsu 1979), to achieve cluster-adapted thresholds. The Otsu method is a non-parametric thresholding approach that does not need any control parameter and maximizes the separability between two classes based on a grey-level histogram. Basically, the optimum threshold is the one with the minimum intra-class variance and the maximum inter-class variance. Otsu thresholding is a technique that has been widely used in burned area mapping studies (Amos et al. 2019; Bin et al. 2019; Otón et al. 2021; Roteta et al. 2021).

Before applying the Otsu method and considering the rationale behind it, it is necessary to balance  $B(m,STC)$  and  $UB(m,STC)$  samples to generate a training sample where each of the classes have the same proportion (50%). In the case of the burned sample all the pixels from  $B(m,STC)$  were included, while for the unburned class a selection was carried out since the size of  $UB(m,STC)$  was, in most cases, greater than  $B(m,STC)$ . Therefore, a subsample of  $UB(m,STC)$ , denoted as  $ub(m,STC)$ , was selected based on a stratified random sampling approach. Three strata were defined based on the distance to the nearest  $B(m,STC)$  pixel: stratum A covered from 10 to 5 km, stratum B covered from 5 km to  $R_{AI}$  (i.e. the distance used to construct the STC), and stratum C encompassed pixels closer than  $R_{AI}$  (Figure 6c.2). The subsample was, whenever possible, randomly selected from stratum A. If this stratum does not provide enough pixels, the remaining pixels are randomly selected from stratum B, and so on. The Otsu method was applied to the resultant training sample:  $B(m,STC) \cup ub(m,STC)$ . To ensure the representativeness of the heterogeneity of  $UB(m,STC)$  and, hence, of the threshold ( $TH(m,STC)$ ), this procedure was repeated 500 times. The high number of repetitions ensured a good representation of the normal distribution of  $TH(m,STC)$  and, for that reason,  $TH(m,STC)$  is computed as the average of all the thresholds:

$$TH(m,STC) = \frac{1}{500} \sum_{k=1}^{500} TH_k(m,STC)(B(m,STC) \cup ub_k(m,STC)) \quad (4)$$

The thresholding process is only applied to the  $\Delta NBR2max$  variable. Considering the properties of the NBR2, i.e., high separability between burned and unburned areas as well as homogeneity within the burned patches, it is considered the most suitable variable over which to apply the contextual growing process described in Subsection 3.10.

### 3.9. Estimation of the threshold surface

As a result of the previous step, an adapted threshold of the  $\Delta NBR2max$  variable was obtained for each STC of the tile and month being processed ( $TH(m,STC)$ ). To avoid any anomaly that might derive from the thresholding process and considering the similarity that should be expected among the thresholds of STC spatially close to each other,  $TH(m,STC)$  are combined to obtain the threshold surface ( $TH_s(m,x,y)$ ) (Figure 7). To do that, for every pixel in the tile the weighted average of all the different  $TH(m,STC)$  within a 20 km radius was computed. The weight was determined by the number of PAF of each STC, assuming that the higher the number of PAF, the larger the size of  $B(m,STC)$  and the more representative the  $TH(m,STC)$ .

	<b>Fire_cci</b>		Ref.: Fire_cci_D2.2_ATBD-SYN_v1.1
	<b>Algorithm Theoretical Basis</b>		Issue 1.1      Date 19/05/2023
	<b>Document – SYN</b>		Page 18

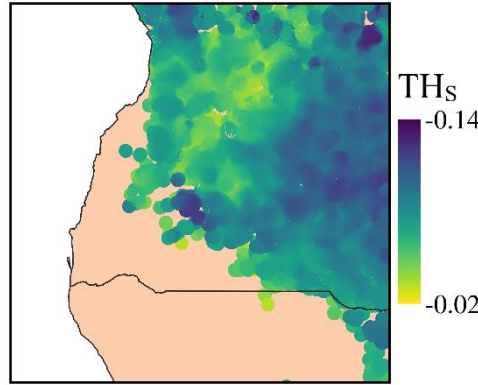


**Figure 7.** Threshold surface ( $TH_s$ ) of the  $\Delta NBR2_{max}$  variable generated for the  $10^\circ \times 10^\circ$  tile, which encompassed the area between  $10^\circ$ - $20^\circ$  E and  $10^\circ$ - $20^\circ$  S, corresponding to September 2019.

Finally, all initial relocated active fires, not just PAF, are compared against the corresponding threshold in  $TH_s(m,x,y)$ . Active fires with a greater spectral change satisfying the condition:  $\Delta NBR2_{max}(m,x',y') < TH_s(m,x',y')$ , are considered as seeds for the posterior contextual growing step. In those occasional cases in which a given PAF does not pass that test, the a priori burned patch that contained the PAF is directly considered as burned in the final burned map, finalising the classification process for that specific PAF.

### 3.10. Generation of the final burned area map

In the final step of the algorithm a contextual growing, which added pixels in an iterative process, is applied to fully detect burned patches and, hence, reduce omission errors. Seeds are used as starting points for the contextual growing, using their corresponding threshold determined by  $TH_s(m,x',y')$  as stopping criteria (Zhang et al. 2005). A pixel is considered as burned if the following conditions are all met:

1. An adjacent grid cell in a queen's case window ( $3 \times 3$ ) must be a seed or a grid cell previously identified as burned
2.  $\Delta NBR2_{max}(m,x,y) < TH_s(m,x',y')$
3.  $S_{max}(m,x,y) \geq 2$
4.  $\sigma_{t,max}(m,x,y) \leq 8$

where  $(x,y)$  represent the location of the pixel being considered and  $(x',y')$  represent the location of the seed from which the growing process started. To avoid problems derived from excessive growing a patch-based filtering process proposed by Lizundia-Loiola et al. (2020) is applied:

- F1. Patches with a quotient between their total number of burned pixels and seeds over 1000 are removed.
- F2. Patches with a quotient between the number of burned pixels located closer than the area of influence ( $R_{AI}$ ) from the seeds and their total number of burned pixels below 0.1 (10%) are removed.
- F3. Contiguous patches to burned patches are removed if they do not contain active fires and are connected by a 1-pixel width connection to the actual burned

	<b>Fire_cci</b> <b>Algorithm Theoretical Basis</b> <b>Document – SYN</b>		Ref.:	Fire_cci_D2.2_ATBD-SYN_v1.1		
			Issue	1.1	Date	19/05/2023
					Page	19

patch. This last filter avoids cases where burned areas are falsely connected to unburned areas with high NBR2 changes.

### 3.11. Uncertainty characterization

Uncertainty characterization of Earth Observation data has been increasingly required by the scientific community of climate and atmosphere modellers. However, both standard approaches proposed by the Joint Committee for Guides in Metrology (2008a, b) fail to provide an appropriate uncertainty propagation framework for FireCCIS311, because analytical methods are not feasible in the case of threshold-based categorisation algorithms (Merchant et al. 2017), and Monte Carlo simulations of large datasets require huge computational resources.

In the case of the FireCCIS311 algorithm, uncertainty was simulated using a clustering approach, which generated a look-up table (LUT) of representative spatiotemporal patterns derived from four predictive variables used by the burned area mapping algorithm. The LUT comprises two dimensions: the spatiotemporal patterns and the predictive variables. The latter dimension consists of a number of intermediate processing variables that can serve as a proxy to characterize the uncertainty of pixels belonging to each specific spatiotemporal pattern. In the resulting BA product, the main input variable considered is the NBR2 index, but in the processing, we are mainly interested in its absolute drop  $\Delta NBR2_{max}$ , which can be calculated based on the difference between the post- and the pre-average (eight pre- and eight post-compositing day observations). The rationale behind including this variable is that burned pixels show a remarkable decrease of NBR2 that lasts a considerable period, and therefore, the lower the value of NBR2 absolute drop, the more probable is the pixel to be actually burned. Moreover, most of thresholds and operations applied by the FireCCIS311 algorithm involve the use of that layer. The separability  $S_{max}$  is another important parameter as the compositing process relies on it. A high value of separability indicates that is very likely to be due to fire event as a rapid change in the index time-series (NBR2 in our case) will yield a separability of large magnitude (Giglio et al. 2009), but to complement this information, the difference between the day of maximum separability and the day of the nearest preliminary seed ( $\Delta t_{PAF}$ ) should be also taken into account. Ideally, this difference should be very small in the case of burn. The last parameter to consider is related to the temporal compactness of burned patches. This layer is important in the sense that neighbouring burned pixels are ideally very close in terms of date of burn forming a burned patch. To characterise this concept, we consider the temporal texture  $\sigma_{t,max}$  (Giglio et al. 2009), computed using the standard deviation between the Julian day of the pixel under consideration, which is considered as the centre of the series, and its neighbouring pixels (rook's case). Figure 8 illustrates an example of the four variables. It can be noticed that all of them indicate more or less the extent of the burned area.

In that way, each pixel can be characterised by a monthly vector of four variables  $v = (\Delta NBR2_{max}, S_{max}, \Delta t_{PAF}, \sigma_{t,max})$ . In the next step, the validation results of the product for the year 2019 (see Stroppiana et al. 2022, Section 2.4.3.2) are considered in order to assign another two variables (burned or unburned in reference and algorithm classifications, respectively) to each pixel. At the end of this stage, each pixel is characterised by a set of six variables (Table 1). As stated earlier, the objective is to create representative spatiotemporal patterns (SP) based on clustering analysis and for that purpose, the *k-means* algorithm was employed (Steinley 2006).

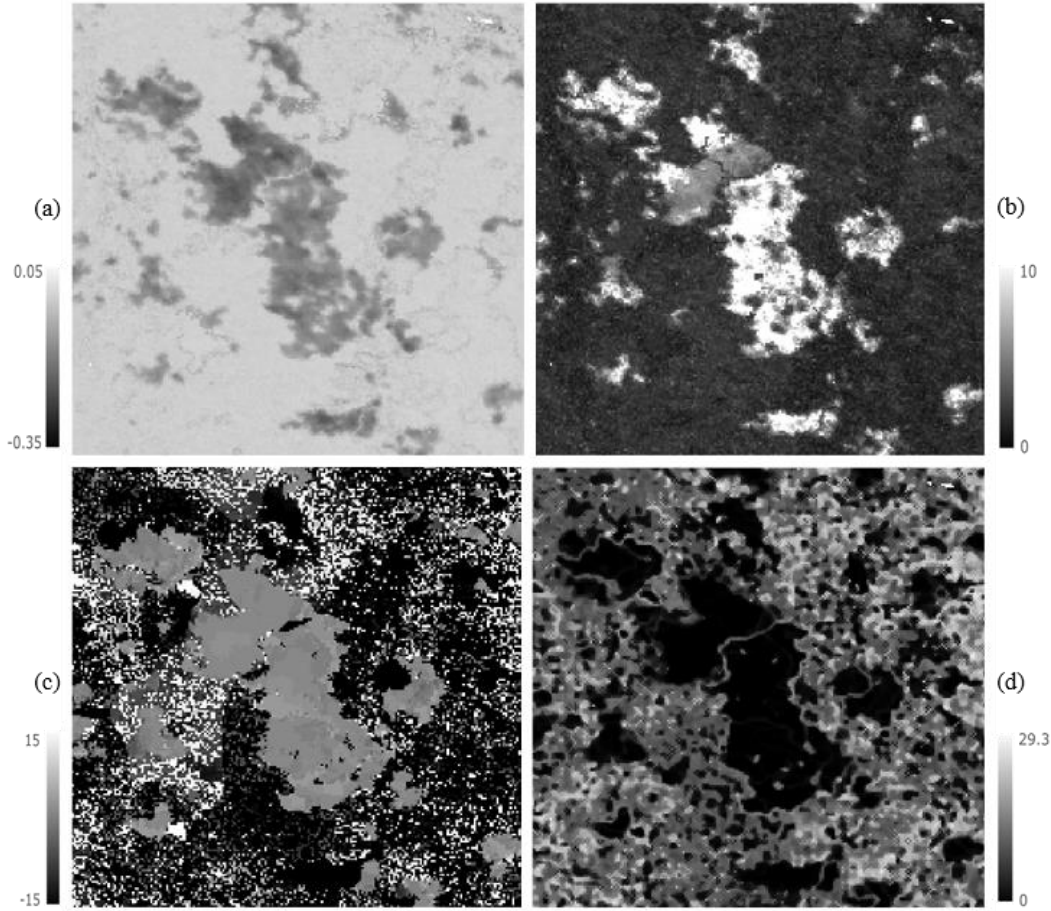


**Figure 8.** Example of predictive variables of uncertainty of FireCCIS310: (a)  $\Delta NBR2_{max}$ ; (b)  $S_{max}$ ; (c)  $\Delta t_{PAF}$ ; (d)  $\sigma_{t,max}$

The clustering is based on the four selected variables, and by using the BA algorithm outputs and the reference, one can compute from the N cases belonging to a spatiotemporal pattern SP, four metrics of the accuracy matrix: True Positive (TP), False Positive (FP), True Negative (TN) and False Negative (FN). The output of this step is illustrated in Table 1.

**Table 1.** Example of a spatiotemporal pattern P of the look-up table

Variables					Classification	
	$Abs\Delta NBR2$	$MaxSep$	$DoyMaxSep$	$Tex$	Reference	Algorithm
Pixel 1	$X_{11}$	$X_{12}$	$X_{13}$	$X_{14}$	B or UB	B or UB
Pixel 2	$X_{21}$	$X_{22}$	$X_{23}$	$X_{24}$	B or UB	B or UB
Pixel 3	$X_{31}$	$X_{32}$	$X_{33}$	$X_{34}$	B or UB	B or UB
Pixel 4	$X_{41}$	$X_{42}$	$X_{43}$	$X_{44}$	B or UB	B or UB
...	...	...	...	...	...	...
Pixel N	$X_{N1}$	$X_{N2}$	$X_{N3}$	$X_{N4}$	B or UB	B or UB
<b>Spatiotemporal pattern P</b>	$X_1$	$X_2$	$X_3$	$X_4$	$\begin{bmatrix} TP & FP \\ FN & TN \end{bmatrix}$	

The confusion matrices of that set of representative patterns allowed computing the probability of burn of each pixel depending on its classification (B or UB). The probability of burn of pixels that were classified as burned was computed using the

precision index whereas the false omission rate was used for pixels classified as unburned. The former expressed the proportion of correct positive prediction (TP) within the pattern (the negative ones are denoted as TN), while the latter indicated the proportion of false negative predictions (FN, false positives FP). The two probabilities were estimated as:

$$P_B = \frac{TP}{TP + FP} * 100 \quad (5)$$

$$P_{UB} = \frac{FN}{TN + FN} * 100 \quad (6)$$

where  $P_B$  denotes the probability of burn of pixels classified as burned by FireCCIS311, and  $P_{UB}$  denotes the probability of burn of pixels classified as unburned.


Figure 9 illustrates an example of a burn probability map. Most of the pixels that correspond to commission errors (FP) show a low probability of burn as they correspond to patterns with a low precision index. On the other hand, the enhancement of burn probability was slightly less observed in the case of omitted pixels (FN).

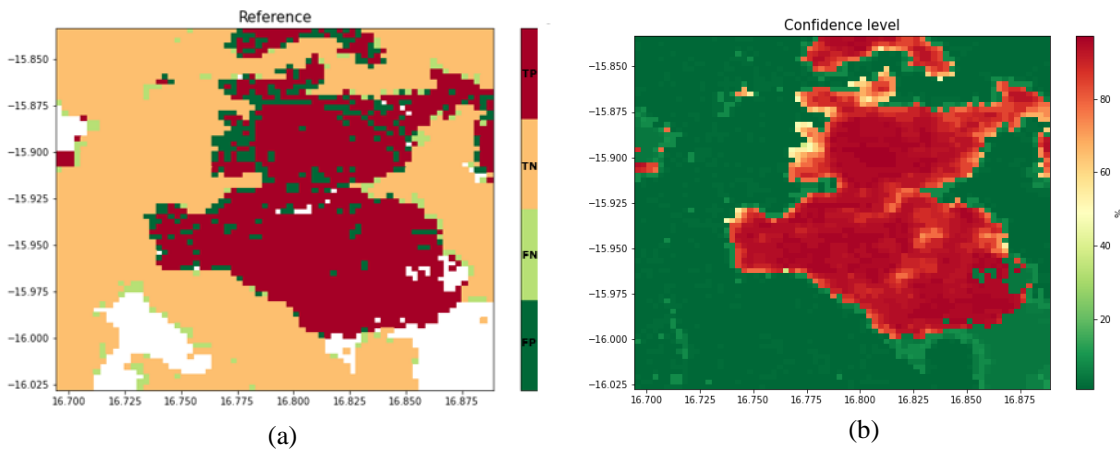


**Figure 9.** Comparison between (a) Reference data and (b) Probability of burn of an area of the tile h19v10 (Angola) for August 2019.

### 3.12. Date of first detection

To assign to each burned pixel the date of the first fire detection (also called the day of the year – DoY, or Julian Day – JD), the date of the composite was used. The composites were based on the day in which the separability index ( $S$ ) was the maximum. This day represents the highest change and therefore the most probable day of burn. Figure 10 illustrates examples of the first fire detection in two different regions with different fire seasons for the year 2019.

	<b>Fire_cci</b> <b>Algorithm Theoretical Basis</b> <b>Document – SYN</b>	Ref.:	Fire_cci_D2.2_ATBD-SYN_v1.1		
		Issue	1.1	Date	19/05/2023
				Page	22

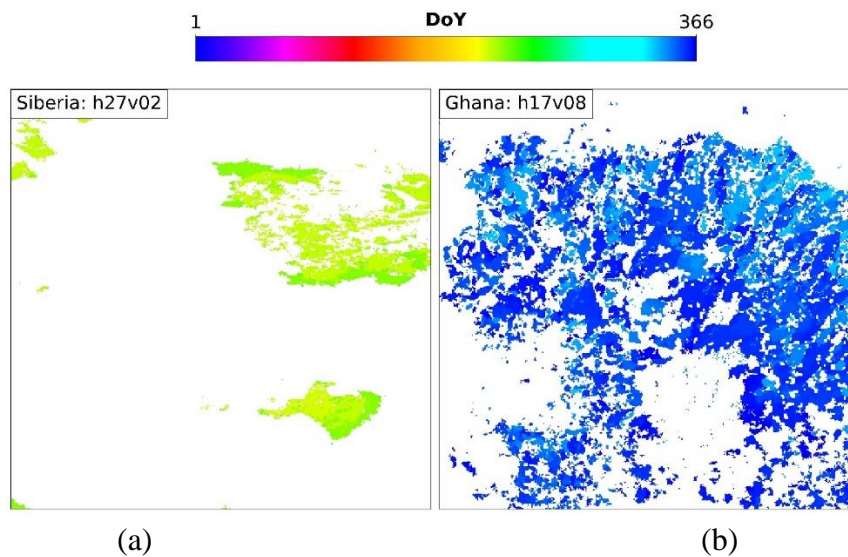


**Figure 10:** (a) Dates of detection of an area of tile h27v02 (Siberia) burned in August. (b) Dates of detection of an area of tile h19v10 (Ghana) burned in December.

### 3.13. Current issues and developments of the algorithm

The monthly composites of  $S$  index included the last 15 days of the previous month ( $m-1$ ) and the first 15 days of the following month ( $m+1$ ) in order to avoid artificially splitting fires that took place at the end or beginning of a month. In that way, the algorithm detects BA of the processing month and also some burned pixels of months  $m-1$  and  $m+1$ , which were reassigned to the corresponding month file. However, sometimes the algorithm detected burn signals at the end/beginning of months  $m-2$  and  $m+2$ , which caused some errors in burn date assignment in version 1.0 of the SYN algorithm. The current version (FireCCIS311) corrects this behaviour and removes these burn cases as they are inconsistent.

Sometimes, the user interested in using the uncertainty information (burn probability) might encounter high probabilities in two successive months. This behaviour corresponds to the case when the algorithm detects burned pixels in month  $m-1$  or  $m+1$ . The date of burn is reassigned to the corresponding month as well as the uncertainty; however, the uncertainty of the processing month is also kept the same. The rationale behind this choice is that the uncertainty estimation is based on predictive variables derived from the processed time-series of that specific month and therefore the replacement by any other value (potentially a value of an unburned pixel) might be considered as an artificial modification of the algorithm result.

## 4. Formatting BA output data to PSD-compliant products

### 4.1. Pixel product

#### 4.1.1. Binning

The pixel products are stitched products, which consist of the results of the BA algorithm. They follow the Product Specification Document (PSD) (Pettinari 2022). Six zones have been defined for which the pixel products are created: North and South America, Europe, Africa, Asia, and Australia. They keep the resolution of 300 m/pixel, but the grids differ, so the pixel values cannot be directly copied from source to target. Instead, the pixel

products are created using the binning technique, which has been defined by NASA and is described in Hooker et al. (1995). This technique is a fundamental part of the Calvalus system (Calvalus software user manual, 2017), and allows to aggregate multiple input images spatially and temporally, thus creating aggregated (so-called L3) maps.

The pixel products are composites computed by temporally aggregating BA pixels into spatial equal-area bins (binning). Bin cells in a pixel product are arranged in an integerised, sinusoidal grid (ISIN), which is compatible to the one used for ESA MERIS L3 products and the MODIS L3 products generated by NASA’s Ocean Biology Processing Group (OBPG). After the temporal and spatial aggregation is done, the data is re-projected onto a configurable target grid – in our case, this is a geographic lat/lon grid of 0.00277778 degrees (approximately 300 m at the Equator). A complete description of the L3 generation methodology can be found in Hooker et al. (1995). Figure 11 depicts the processing scenario.

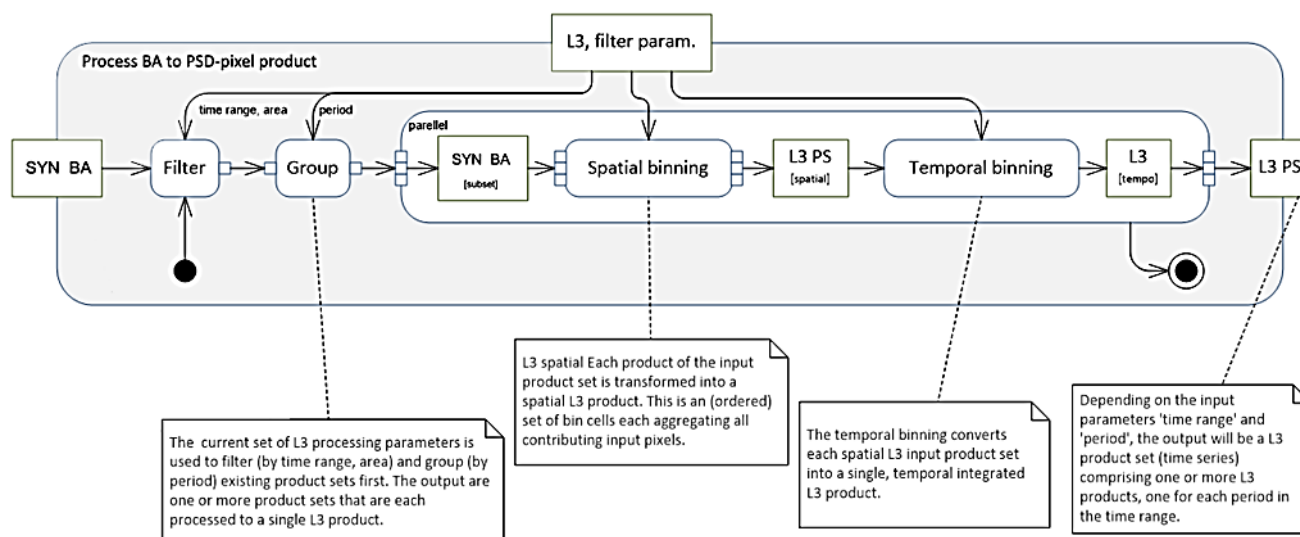


**Figure 11:** Calvalus L3 processing

It is noteworthy that spatial binning and temporal binning employ a specific piece of software, the so-called aggregator. Basically, an aggregator provides strategies for spatial and temporal binning. Operating on single bin cells, an aggregator provides the answers for:

- Spatial binning: how are input samples of a single observation (swath) aggregated to spatial bins?
- Temporal binning: how are spatial bins aggregated to temporal bins?
- Final statistics: how are final statistics computed?

#### 4.1.2. The JDAggregator

There are multiple built-in aggregators in Calvalus, such as an aggregator that computes a mean value of the input data, or another one that computes the min and max values of the input data. For the aggregation of the SYN BA data, a dedicated aggregator has been newly developed by adapting the MODIS one (ModisJDAggregator). This aggregator produces two of the three image layers the pixel products consist of: JD (the day of the year of the first detection of the fire) and CL (the confidence level of the burn detection referring to the probability of burn calculated in Subsection 3.11). The third layer, LC

(which is the land cover class, according to the PSD), is computed in a dedicated finalisation step, which is described in Subsection 4.1.3.

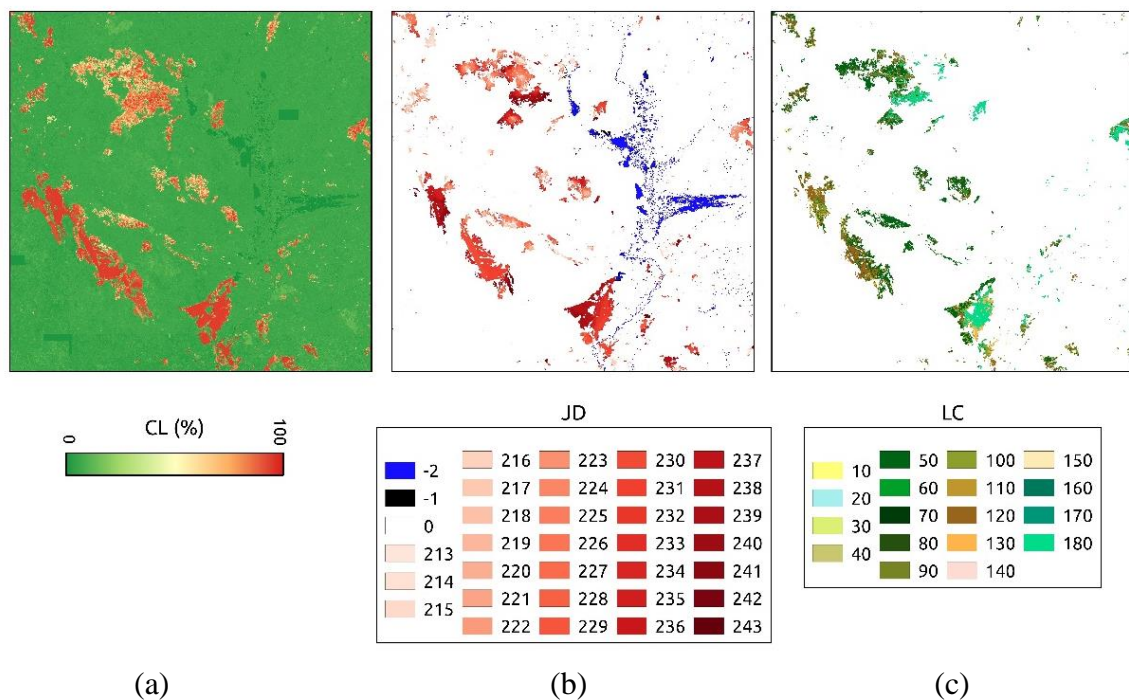
The JDAggregator does only a spatial aggregation, as the processing is configured to use only those BA products from the month which is aggregated; so, if the processing task is to create the pixel product for January 2019, only input data from January 2019 is considered. The spatial aggregation is done as follows:

$$JD(t_{period}) = \begin{cases} \text{Min}(jd(p, t) \text{ with } t \text{ in } t_{period} \text{ and } jd(t) \neq 0 \\ b \text{ is the fill\_value} \end{cases} \quad (7)$$

A valid JD value is considered to be set if it is positive and within the considered month. If multiple observations contribute to a single bin cell, the values of one of these observations are used for the whole bin cell. The preferred observation is the one with the lowest JD value that is within the considered month, indicating the earliest day of burn. The bin cell is assigned the JD value and the CL value of that observation.

#### 4.1.3. Finalisation

In order to create the LC image layer and the metadata, a finalisation step is run after the binning step. This step takes as input the result of Subsection 4.1.1. For each pixel, the process checks if the pixel is in a burnable class and does the respective re-mapping: if the pixel is reported to have burned, but the respective LC class of that pixel is unburnable, the JD value of the pixel is changed to -2 (unburnable). The same is done for the confidence level: if the pixel is reported to have burned, but the respective LC class of that pixel is not burnable, the CL value of the pixel is changed to 0. These cases could happen due to the re-projection from the sinusoidal projection of the BA algorithm to the geographical coordinates of the PSD-compliant product. Also, the LC class is set to each burned pixel; in other pixels, it is set to 0. A value of -1 is assigned to non-observed areas. Figure 12 illustrates an example of the different layers generated at 300 m pixels.





	<b>Fire_cci</b> <b>Algorithm Theoretical Basis</b> <b>Document – SYN</b>	Ref.:	Fire_cci_D2.2_ATBD-SYN_v1.1			
		Issue	1.1	Date	19/05/2023	
					Page	25

**Figure 12:** Example of the final layers generated at full pixel resolution for fires occurred in the southern border of Brazil and Bolivia in 2019: (a) Confidence Level (CL) (b) Julian day of detection (JD). (b) Burned Land Cover class (LC).

## 4.2. Grid product

The grid products are global products which aggregate the result of the BA algorithm onto a 0.25°-pixel grid. Hence, the pixels in the result of the BA algorithm cannot simply be copied but need some aggregation.

The layers created for the grid product are the sum of BA, the standard error of the burned area, the fraction of the observed area, the fraction of burnable area, and the sum of burned area of each land cover class. In the following sections, it is explained how these layers are derived from the BA algorithm result and LC data.

### 4.2.1. Sum of burned area

The sum of burned area  $A_{burned}$  is given in m<sup>2</sup>, and is defined as follows:

$$A_{burned}(c, t_{period}) = \sum_{sp \in c} A(sp \cap c | t_{period}, burnable(LC), burned(t_{period})) \quad (8)$$

where:  $c$  is the target grid cell,  $t_{period}$  is the requested time period,  $sp$  is a source pixel and  $A$  is the area segment of the source pixel relating to the target grid cell. The area segment is only considered for the computation of the sum of burned area if it has burned in the requested time period and the corresponding land cover class is identified as a burnable surface.

The product detected  $4.99 \times 10^6$  km<sup>2</sup> globally for the year 2019. Most of the burned area was concentrated in the tropical savanna biome of the African continent (Figure 13).

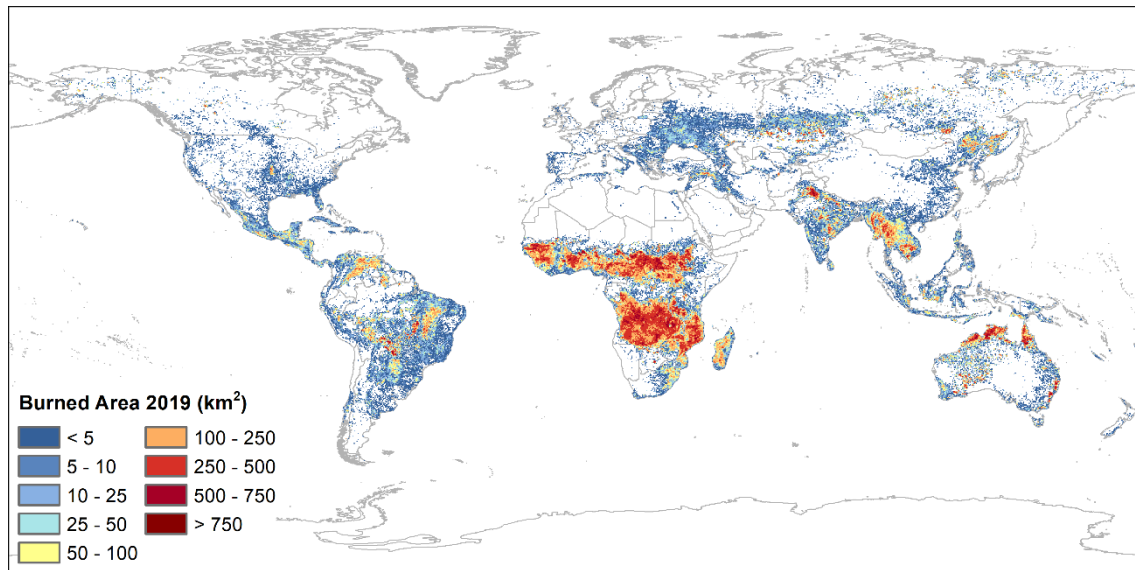


**Figure 13.** Burned area (km<sup>2</sup>) of the year 2019 detected by the FireCCIS311 product at 0.25° spatial resolution.

	<b>Fire_cci</b>		Ref.: Fire_cci_D2.2_ATBD-SYN_v1.1
	<b>Algorithm Theoretical Basis</b>		Issue 1.1      Date 19/05/2023
	<b>Document – SYN</b>		Page 26

#### 4.2.2. Ancillary variables

##### a. Standard error

The standard error is also given in units of m<sup>2</sup>. It is computed after the burned area has been identified, on the basis of the confidence level of each source pixel ( $CL_{sp}$ ). The standard error is aggregated following these steps:

1. Only those burnable source pixels that were observed (burned or unburned) in the given  $t_{period}$  and grid cell  $c$  are taken into account:

$$if CL_{sp} > 0 \text{ and } sp \cap c | t_{period} \quad (9)$$

2. The confidence level (Subsection 3.11), since it is expressed in %, is scaled between 0 and 1, dividing the confidence level by 100:

$$pb_{sp_i} = CL_{sp_i} / 100 \quad (10)$$

where  $sp_i$  represents any source pixel that met the previous conditions.

3. The variance of the given grid cell is calculated:

$$Var_c = \sum_{i=1}^n pb_{sp_i} \cdot (1 - pb_{sp_i}) \quad (11)$$

$pb_{sp_i}$  represents the probabilities of step 2,  $n$  are all the  $sp$  that contribute to the  $Var_c$ , that is, those that met the step 1 conditions, and  $c$  is the target grid cell.

4. The standard error of the given grid cell is calculated:

$$SE_c = \sqrt{Var_c \cdot \left(\frac{n}{n-1}\right)} \cdot pixel\_area_{sp} \quad (12)$$

where  $Var_c$  is the variance of the grid cell  $c$ ,  $n$  the same as step 3,  $c$  the target grid cell, and  $pixel\_area_{sp}$  is the mean pixel area of an  $sp$  within  $c$ .

##### b. Fraction of burnable area

The fraction of burnable area (FBA) is given as a unitless value between 0 and 1, where a pixel value of 1 indicates that the whole area covered by the grid cell consists of burnable pixels, as indicated by the Land Cover classification map, while a value of 0 indicates that no source pixels of the area covered by the grid cell are burnable and is defined as follows:

$$FBA(c, t_{period}) = \frac{\sum_{sp \in c} A(sp \cap c | t_{period}, burnable(LC))}{A(c)} \quad (13)$$

where:  $c$  is the target grid cell,  $t_{period}$  is the requested time period,  $sp$  is a source pixel,  $A$  is the area segment of the source pixel relating to the target grid cell and  $A(c)$  denotes the

	<b>Fire_cci</b> <b>Algorithm Theoretical Basis</b> <b>Document – SYN</b>	Ref.:	Fire_cci_D2.2_ATBD-SYN_v1.1		
		Issue	1.1	Date	19/05/2023
				Page	27

area of the target grid cell. The area segment is only considered for the computation of the fraction of burnable area if the corresponding land cover class (LC) of  $sp$  is identified as a burnable surface.

### c. Fraction of observed area

The fraction of observed area (FOA) is given as a unitless value between 0 and 1, where a grid cell value of 1 indicates that the whole burnable area covered by the grid cell has been observed, while a value of 0 indicates that no source pixels of the burnable area covered by the grid cell have been observed, and is defined as follows:

$$FOA(c, t_{period}) = \frac{\sum_{sp \in c} A(sp \cap c | t_{period}, burnable(LC), p(sp) = 1)}{Burnable A(c)} \quad (14)$$

where:  $c$  is the target grid cell,  $t_{period}$  is the requested time period,  $sp$  is a source pixel,  $A$  is the area segment of the source pixel relating to the target grid cell and  $Burnable A(c)$  denotes the burnable area of the target grid cell. The area segment is only considered for the computation of fraction of observed area if it is burnable and it has been observed in the requested time period and for the requested grid cell.

### d. Sum of BA of each LC class

The sum of BA in each land cover class ( $A_{LC}$ ) allows differentiation between the burned area corresponding to each land cover, for emissions calculation purposes. For each LC class, it is defined as follows:

$$A_{LC}(c, t_{period}, LC) = \sum_{sp \in c} A(sp \cap c | t_{period}, burnable(LC), burned(t_{period}), LC) \quad (15)$$


where:  $c$  is the target grid cell,  $t_{period}$  is the requested time period,  $sp$  is a source pixel,  $A$  is the area segment of the source pixel relating to the target grid cell. The area segment is only considered for the computation of the sum of burned area if it is a burnable land cover, has burned in the requested time period, is in the requested grid cell and it has also the corresponding land cover class.

## 5. References

- Alonso-Canas, I., & Chuvieco, E. (2015). Global Burned Area Mapping from ENVISAT-MERIS data Remote Sensing of Environment, Remote Sensing of Environment, 163, 140-152.
- Amos, C., Petropoulos, G.P., & Ferentinis, K.P. (2019). Determining the use of Sentinel-2A MSI for wildfire burning & severity detection. International journal of remote sensing, 40, 905-930
- Astola, J., & Kuosmanen, P. (1997). Fundamentals of Nonlinear Digital Filtering (1st ed.). CRC Press
- Barbosa, P.M., Pereira, J.M.C., & Grégoire, J.M. (1998). Compositing criteria for burned area assessment using multitemporal low resolution satellite data. Remote Sensing of Environment, 65, 38-49
- Bastarrika, A., Chuvieco, E., & Martín, M.P. (2011). Mapping burned areas from Landsat

	<b>Fire_cci</b> <b>Algorithm Theoretical Basis</b> <b>Document – SYN</b>	Ref.:	Fire_cci_D2.2_ATBD-SYN_v1.1		
		Issue	1.1	Date	19/05/2023
				Page	28

- TM/ETM+ data with a two-phase algorithm: balancing omission and commission errors. *Remote Sensing of Environment*, 115, 1003-1012
- Bin, W., Ming, L., Dan, J., Suju, L., Qiang, C., Chao, W., Yang, Z., Huan, Y., & Jun, Z. (2019). A Method of Automatically Extracting Forest Fire Burned Areas Using Gf-1 Remote Sensing Images. In *IGARSS 2019 - 2019 IEEE International Geoscience and Remote Sensing Symposium* (pp. 9953-9955)
- Boschetti, L., Roy, D.P., Justice, C.O., & Giglio, L. (2010). Global assessment of the temporal reporting accuracy and precision of the MODIS burned area product. *International Journal of Wildland Fire*, 19, 705-709
- Brassel, K.E., & Reif, D. (1979). A procedure to generate Thiessen polygons. *Geographical Analysis*, 11, 289-303
- Calvalus – software user manual (2017). *Cal/Val and User Services – Calvalus Software User Manual Version 1.7* 19. December 2017 – available on request
- Campagnolo, M.L., Oom, D., Padilla, M., & Pereira, J.M.C. (2019). A patch-based algorithm for global and daily burned area mapping. *Remote Sensing of Environment*, 232, 111288
- Chuvieco, E., Ventura, G., Martín, M.P., & Gomez, I. (2005). Assessment of multitemporal compositing techniques of MODIS and AVHRR images for burned land mapping. *Remote Sensing of Environment*, 94, 450 – 462
- Chuvieco, E., Yue, C., Heil, A., Mouillot, F., Alonso-Canas, I., Padilla, M., Pereira, J.M., Oom, D., Tansey, K. (2016). A new global burned area product for climate assessment of fire impacts. *Global Ecology and Biogeography* 25, 619-629
- Chuvieco, E., Lizundia-Loiola, J., Pettinari, M.L., Ramo, R., Padilla, M., Tansey, K., Mouillot, F., Laurent, P., Storm, T., Heil, A., Plummer, S. (2018) Generation and analysis of a new global burned area product based on MODIS 250 m reflectance bands and thermal anomalies. *Earth System Science Data* 10, 2015-2031
- Defourny, P., Lamarche, C., Bontemps, S., De Maet, T., Van Bogaert, E., Moreau, I., Brockmann, C., Boettcher, M., Kirches, G., Wevers, J., Santoro, M., Ramoino, F., Arino, O., 2017. *Land Cover Climate Change Initiative - Product User Guide v2. Issue 2.0*. Available at: [http://maps.elie.ucl.ac.be/CCI/viewer/download/ESACCI-LC-Ph2-PUGv2\\_2.0.pdf](http://maps.elie.ucl.ac.be/CCI/viewer/download/ESACCI-LC-Ph2-PUGv2_2.0.pdf) (last accessed on January 2023)
- Dice, L.R. (1945). Measures of the Amount of Ecologic Association Between Species. *Ecology*, 26, 297-302
- Dinerstein, E., Olson, D., Joshi, A., Vynne, C., Burgess, N.D., Wikramanayake, E., Hahn, N., Palminteri, S., Hedao, P., Noss, R., Hansen, M., Locke, H., Ellis, E.C., Jones, B., Barber, C.V., Hayes, R., Kormos, C., Martin, V., Crist, E., Sechrest, W., Price, L., Baillie, J.E.M., Weeden, D., Suckling, K., Davis, C., Sizer, N., Moore, R., Thau, D., Birch, T., Potapov, P., Turubanova, S., Tyukavina, A., de Souza, N., Pintea, L., Brito, J.C., Llewellyn, O.A., Miller, A.G., Patzelt, A., Ghazanfar, S.A., Timberlake, J., Kloser, H., Shennan-Farpon, Y., Kindt, R., Lilleso, J.B., van Breugel, P., Graudal, L., Voge, M., Al-Shammari, K.F., & Saleem, M. (2017). An Ecoregion-Based Approach to Protecting Half the Terrestrial Realm. *BioScience*, 67, 534-545
- Franquesa, M., Vanderhoof, M.K., Stavrakoudis, D., Gitas, I.Z., Roteta, E., Padilla, M., & Chuvieco, E. (2020). Development of a standard database of reference sites for

	<b>Fire_cci</b> <b>Algorithm Theoretical Basis</b> <b>Document – SYN</b>	Ref.:	Fire_cci_D2.2_ATBD-SYN_v1.1		
		Issue	1.1	Date	19/05/2023
				Page	29

- validating global burned area products. *Earth System Science Data*, 12, 3229-3246
- Franquesa, M., Lizundia-loiola, J., Stehman, S.V., & Chuvieco, E. (2022). Using long temporal reference units to assess the spatial accuracy of global satellite-derived burned area products. *Remote Sensing of Environment*, 269, 112823
- Giglio, L., Boschetti, L., Roy, D.P., Humber, M.L., & Justice, C.O. (2018). The Collection 6 MODIS burned area mapping algorithm and product. *Remote Sensing of Environment*, 217, 72-85
- Giglio, L., Loboda, T., Roy, D.P., Quayle, B., & Justice, C.O. (2009). An active-fire based burned area mapping algorithm for the MODIS sensor. *Remote Sensing of Environment*, 113, 408-420
- Giglio, L., Schroeder, W., Justice, C.O. (2016) The collection 6 MODIS active fire detection algorithm and fire products. *Remote Sensing of Environment* 178, 31-41
- Hooker, S. B., Firestone, E.R., Acker, J. G., Campbell, J. W. Blaisdell, J. M., Darzi, M. (1995). NASA Technical Memorandum 104566, Volume 32: Level-3 SeaWiFS data product – Spatial and temporal binning algorithms. SeaWiFS technical report series. NASA Goddard Space Flight Center; Greenbelt, MD, United States. Available at: [https://oceancolor.gsfc.nasa.gov/SeaWiFS/TECH\\_REPORTS/PreLPDF/PreLVol32.pdf](https://oceancolor.gsfc.nasa.gov/SeaWiFS/TECH_REPORTS/PreLPDF/PreLVol32.pdf) (last access: January 2023)
- Joint Committee for Guides in Metrology (2008a). Evaluation of measurement data – Guide to the expression of uncertainty in measurement, JCGM 100:2008, available at: <http://www.bipm.org/en/publications/guides/gum.html> (last access: January 2023)
- Joint Committee for Guides in Metrology (2008b). Evaluation of measurement data – Supplement 1 to the “Guide to the expression of uncertainty in measurement” – Propagation of distributions using a Monte Carlo method, JCGM 101:2008, available at: <http://www.bipm.org/en/publications/guides/gum.html> (last access: January 2023)
- Liu, J., Maeda, E.E., Wang, D., & Heiskanen, J. (2021). Sensitivity of Spectral Indices on Burned Area Detection using Landsat Time Series in Savannas of Southern Burkina Faso. *Remote Sensing*, 13
- Lizundia-Loiola, J., Otón, G., Ramo, R., & Chuvieco, E. (2020). A spatiotemporal active-fire clustering approach for global burned area mapping at 250 m from MODIS data. *Remote Sensing of Environment*, 236, 111493
- Lizundia-Loiola, J., Franquesa, M., Boettcher, M., Kirches, G., Pettinari, M.L., & Chuvieco, E. (2021). Implementation of the Burned Area Component of the Copernicus Climate Change Service: From MODIS to OLCI Data. *Remote Sensing*, 13
- Lizundia-Loiola, J., Franquesa, M., Khairoun, A., & Chuvieco, E. (2022). Global burned area mapping from Sentinel-3 Synergy and VIIRS active fires. *Remote Sensing of Environment*, 282, 113298
- Merchant, C.J., Paul, F., Popp, T., Ablain, M., Bontemps, S., Defourny, P., Hollmann, R., Lavergne, T., Laeng, A., de Leeuw, G., Mittaz, J., Poulsen, C., Povey, A.C., Reuter, M., Sathyendranath, S., Sandven, S., Sofieva, V.F., & Wagner, W. (2017). Uncertainty information in climate data records from Earth observation. *Earth System Science Data*, 9, 511-527
- Oliva, P., & Schroeder, W. (2015). Assessment of VIIRS 375 m active fire detection


	<b>Fire_cci</b> <b>Algorithm Theoretical Basis</b> <b>Document – SYN</b>	Ref.:	Fire_cci_D2.2_ATBD-SYN_v1.1		
		Issue	1.1	Date	19/05/2023
				Page	30

- product for direct burned area mapping. *Remote Sensing of Environment*, 160, 144-155
- Otón, G., Lizundia-Loiola, J., Pettinari, M.L., & Chuvieco, E. (2021). Development of a consistent global long-term burned area product (1982–2018) based on AVHRR-LTDR data. *International Journal of Applied Earth Observation and Geoinformation*, 103, 102473
- Otsu, N. (1979). A Threshold Selection Method from Gray-Level Histograms. *IEEE Transactions on Systems, Man, and Cybernetics*, 9, 62-66
- Padilla, M., Olofsson, P., Stehman, S.V., Tansey, K., & Chuvieco, E. (2017). Stratification and sample allocation for reference burned area data. *Remote Sensing of Environment*, 203, 240-255
- Pettinari M.L. (2022) ESA CCI ECV Fire Disturbance: D1.2 Product Specification Document, versión 7.1. Available at: <https://climate.esa.int/en/projects/fire/key-documents/>
- Roteta, E., Bastarrika, A., Padilla, M., Storm, T., & Chuvieco, E. (2019). Development of a Sentinel-2 burned area algorithm: Generation of a small fire database for sub-Saharan Africa. *Remote Sensing of Environment*, 222, 1-17
- Roteta, E., Bastarrika, A., Franquesa, M., & Chuvieco, E. (2021). Landsat and sentinel-2 based burned area mapping tools in google earth engine. *Remote Sensing*, 13, 1-30
- Schroeder, W., Giglio, L., (2018). Visible Infrared Imaging Radiometer Suite (VIIRS) 375 m & 750 m active fire products. In: *Product User's Guide Version 1.4. NASA VIIRS Land Science Investigator Processing System (SIPS)*.
- Schroeder, W., Oliva, P., Giglio, L., Csiszar, I.A. (2014). The New VIIRS 375 m active fire detection data product: Algorithm description and initial assessment. *Remote Sensing of Environment*, 143, 85-96
- Sousa, A.M.O., Pereira, J.M.C., & Silva, J.M.N. (2003). Evaluating the performance of multitemporal image compositing algorithms for burned area analysis. *International Journal of Remote Sensing*, 24, 1219–1236
- Steinley, Douglas L. (2006). K-means clustering: a half-century synthesis. *The British journal of mathematical and statistical psychology* 59 Pt 1: 1-34.
- Stroppiana D., Sali M., Boschetti M., Busetto L., Ranghetti L., Franquesa M., Lizundia-Loiola J., Pettinari M.L. (2022) ESA CCI ECV Fire Disturbance: D4.1 Product Validation and Intercomparison Report, version 2.1. Available at: <https://climate.esa.int/en/projects/fire/key-documents/>
- Trigg, S., Flasse, S., 2001. An evaluation of different bi-spectral spaces for discriminating burned shrub-savannah. *International Journal of Remote Sensing*. 22, 2641–2647
- Waigl, C.F., Stuefer, M., Prakash, A., & Ichoku, C. (2017). Detecting high and low-intensity fires in Alaska using VIIRS I-band data: An improved operational approach for high latitudes. *Remote Sensing of Environment*, 199, 389-400
- Zhang, Q.F., Pavlic, G., Chen, W.J., Fraser, R., Leblanc, S., & Cihlar, J. (2005). A semi-automatic segmentation procedure for feature extraction in remotely sensed imagery. *Computers & Geosciences*, 31, 289-296

	<b>Fire_cci</b>		Ref.: Fire_cci_D2.2_ATBD-SYN_v1.1
	<b>Algorithm Theoretical Basis</b>		Issue 1.1      Date 19/05/2023
	<b>Document – SYN</b>		Page 31

## Annex 1: Acronyms and abbreviations

ATBD	Algorithm Theoretical Basis Document
ASCII	American Standard Code for Information Interchange
B	Burned sample
BA	Burned Area
CCI	Climate Change Initiative
Ce	Commission error
CL	Confidence Level
DC	Dice Coefficient
DoY	Day of the Year
ECV	Essential Climate Variables
ESA	European Space Agency
FAO	The Food and Agriculture Organization
FBA	Fraction of Burnable Area
FN	False Negative
FOA	Fraction of Observable Area
FP	False Positive
GCOS	Global Climate Observing System
IPCC	Intergovernmental Panel on Climate Change
ISIN	Integerised sinusoidal grid
JD	Julian Day, also day of the year of first detection of a fire
L3	Level 3
LC	Land Cover
LCCS	Land Cover Classification System
LUT	Look-Up Table
LSWIR	Long SWIR
MERIS	Medium Resolution Imaging Spectrometer
MODIS	Moderate Resolution Imaging Spectroradiometer
NASA	The National Aeronautics and Space Administration
NBR2	Normalized Burn Ratio 2
NIR	Near InfraRed
OBPG	Ocean Biology Processing Group
Oe	Omission error
OLCI	Ocean and Land Colour Instrument
PAF	Potential Active Fire
PSD	Product Specification Document
R <sub>AI</sub>	Area of influence
relB	Relative Bias
S	Separability index
S3	Sentinel-3

	<b>Fire_cci</b> <b>Algorithm Theoretical Basis</b> <b>Document – SYN</b>		Ref.:	Fire_cci_D2.2_ATBD-SYN_v1.1		
			Issue	1.1	Date	19/05/2023
					Page	32

SLSTR	Sea and Land Surface Temperature Radiometer
SP	Spatiotemporal Pattern
SPOT	Satellite Pour l'Observation de la Terre
S-NPP	Suomi National Polar-orbiting Partnership
STC	Spatiotemporal Cluster
SSWIR	Short SWIR
SWIR	Short Wave InfraRed
SYN	Sentinel-3 Synergy
TH	Threshold
TN	True Negative
TP	True Positive
TSA	Thiessen Scene Area
UB	Unburned sample
VIIRS	Visible Infrared Imaging Radiometer Suite
WRS-2	Worldwide Reference System-2



## Annex 2: Sentinel 3 Synergy (S3 SYN) band characteristics

SYN channels	Central Wavelength (nm)	Width (nm)	Original instrument channel	Function
SYN01	400	15	Oa01	Aerosol correction, improved water constituent retrieval
SYN02	412.5	10	Oa02	Yellow substance and detrital pigments (turbidity)
SYN03	442.5	10	Oa03	Chlorophyll absorption maximum, biogeochemistry, vegetation
SYN04	490	10	Oa04	High Chlorophyll,
SYN05	510	10	Oa05	Chlorophyll, sediment, turbidity, red tide
SYN06	560	10	Oa06	Chlorophyll reference (Chlorophyll minimum)
SYN07	620	10	Oa07	Sediment loading
SYN08	665	10	Oa08	Chlorophyll (2 <sup>nd</sup> Chlorophyll absorption maximum), sediment, yellow substance/vegetation
SYN09	673.75	7.5	Oa09	For improved fluorescence retrieval and to better account for smile together with the bands 665 and 680 nm
SYN10	681.25	7.5	Oa10	Chlorophyll fluorescence peak, red edge
SYN11	708.75	10	Oa11	Chlorophyll fluorescence baseline, red edge transition
SYN12	753.75	7.5	Oa12	O <sub>2</sub> absorption/clouds, vegetation
SYN13	778.75	15	Oa16	Atmospheric correction/aerosol correction
SYN14	865	20	Oa17	Atmospheric correction/aerosol correction, clouds, pixel co-registration
SYN15	885	10	Oa18	Water vapor absorption reference band. Common reference band with SLSTR instrument. Vegetation monitoring



fire  
cci

Fire\_cci  
Algorithm Theoretical Basis  
Document – SYN

Ref.: Fire\_cci\_D2.2\_ATBD-SYN\_v1.1

Issue 1.1

Date 19/05/2023

Page 34

SYN channels	Central Wavelength (nm)	Width (nm)	Original instrument channel	Function
SYN16	1 020	40	Oa21	Atmospheric correction/aerosol correction
SYN17	554.27	20	S1 (nadir view)	Cloud screening, vegetation monitoring, aerosol
SYN18	659.47	20	S2 (nadir view)	NDVI, vegetation monitoring, aerosol
SYN19	868.00	20	S3 (nadir view)	NDVI, cloud flagging, Pixel co-registration
SYN20	1613.40	60	S5 (nadir view)	SWIR1: Cloud clearing, ice, snow, vegetation monitoring
SYN21	2255.70	50	S6 (nadir view)	SWIR2: Vegetation state and cloud clearing
SYN22	1 020	20	S1 (oblique view)	Cloud screening, vegetation monitoring, aerosol
SYN23	554.27	20	S2 (oblique view)	NDVI, vegetation monitoring, aerosol
SYN24	659.47	20	S3 (oblique view)	NDVI, cloud flagging, Pixel co-registration
SYN25	868.00	60	S5 (oblique view)	Short SWIR: Cloud clearing, ice, snow, vegetation monitoring
SYN26	1613.40	50	S6 (oblique view)	Long SWIR: Vegetation state and cloud clearing